5-2014

Parasitic Layer-Based Reconfigurable Antenna and Array for Wireless Applications

Zhouyuan Li
Utah State University

PARASITIC LAYER-BASED RECONFIGURABLE ANTENNA AND ARRAY FOR WIRELESS APPLICATIONS

by

Zhouyuan Li

A dissertation submitted in partial fulfillment
of the requirements for the degree

of

DOCTOR OF PHILOSOPHY

in

Electrical Engineering

Approved:

Dr. Bedri A. Cetiner Major Professor	Dr. Doran J. Baker Committee Member
Dr. Jacob Gunther Committee Member	Dr. Rose Qingyang Hu Committee Member
Dr. T.C. Shen Committee Member	Dr. Mark R. McLellan Vice President for Research and Dean of the School of Graduate Studies

UTAH STATE UNIVERSITY
Logan, Utah

2014

Abstract

Parasitic Layer-Based Reconfigurable Antenna and Array for Wireless Applications

by

Zhouyuan Li, Doctor of Philosophy

Utah State University, 2014

Major Professor: Dr. Bedri A. Cetiner
Department: Electrical and Computer Engineering

This dissertation focuses upon the theoretical analysis and design of smart antennas with reconfigurable radiation properties. The presented multi-functional reconfigurable antennas (MRAs) are aimed to applications in WLAN (wireless local area network) systems. The theoretical analysis of the MRA was first investigated to validate the design concept, and then applied for practical applications. The multi-functional reconfigurable antenna array (MRAA), which is a new class of antenna array, is also created as a linear formation (4×1) of MRA, with theoretical analysis and design of the MRAA fully described. This work developed three MRA(A)s for practical implementation in WLAN systems. The first design is the MRA operating in 802.11 b/g band (2.4-2.5 GHz), with nine beam steering directions in a parasitic layer-based MRA structure. The second is a MRA operating in 802.11ac band (5.17-5.83 GHz) with three beam steering directions in a simplified parasitic layer-based MRA structure. The third is a MRAA extension of the second design. The design process of these MRA(A)s is realized with the joint utilization of electromagnetic (EM) full-wave analysis and multi-objective genetic algorithm. All three MRA(A) designs have been fabricated and measured. The measured and simulated results agree well for both impedance and radiation characteristics. These prototypes can be directly employed in a WLAN system since practical limits have been taken into account with real switches and

components implemented. Finally, this dissertation work concludes with plans for future work, which will focus on development of MRA(A)s with dual-frequency operation.

(96 pages)

Public Abstract

Parasitic Layer-Based Reconfigurable Antenna and Array for Wireless Applications

by

Zhouyuan Li, Doctor of Philosophy

Utah State University, 2014

Major Professor: Dr. Bedri A. Cetiner
Department: Electrical and Computer Engineering

Antenna is one of the most important components in wireless systems since signal transmission and reception are conducted through the antenna interface. Therefore, the signal quality is highly affected by the properties of the antenna. Traditional antennas integrated in devices such as laptops or cell phones have fixed radiation properties and can not be changed to adapt to different environments. Thus the performance of the whole system will be negatively affected since the antenna will not operate in the optimum status in different environments. To solve this problem, reconfigurable antenna, which can dynamically change its operation frequency, radiation pattern, and polarization, has gained a significant interest recently. Reconfigurable antennas are considered smart antennas, and can maximize the capacity of the wireless system. This dissertation focuses upon the theoretical analysis and design of smart antennas with reconfigurable radiation properties. The presented multi-functional reconfigurable antennas (MRAs) are aimed to applications in WLAN (wireless local area network) systems. The theoretical analysis of the MRA was first investigated to validate the design concept, and then applied for practical applications. The multi-functional reconfigurable antenna array (MRAA), which is a new class of antenna array, is also created as a linear formation (4×1) of MRA, with theoretical analysis and design of the MRAA fully described. This work developed three MRA(A)s for practical

implementation in WLAN systems. The first design is the MRA operating in 802.11 b/g band (2.4-2.5 GHz), with nine beam steering directions in a parasitic layer-based MRA structure. The second is a MRA operating in 802.11ac band (5.17-5.83 GHz) with three beam steering directions in a simplified parasitic layer-based MRA structure. The third is a MRAA extension of the second design. The design process of these MRA(A)s is realized with the joint utilization of electromagnetic (EM) full-wave analysis and multi-objective genetic algorithm. All three MRA(A) designs have been fabricated and measured. The measured and simulated results agree well for both impedance and radiation characteristics. These prototypes can be directly employed in a WLAN system since practical limits have been taken into account with real switches and components implemented. Finally, this dissertation work concludes with plans for future work, which will focus on development of MRA(A)s with dual-frequency operation.

Acknowledgments

I would like to take this opportunity to thank all the people who helped through my PhD program. In particular, I want to give special thanks to my advisor, Dr. Cetiner, who guided me all the time and gave me valuable suggestions on my research. Without his continuous support, it would have been impossible to finish my PhD.

I am also grateful to my other committee members, Dr. Baker, Dr. Gunther, Dr. Hu, and Dr. Shen, for their valuable insight on my work.

I also want to thank all the colleagues I worked with during past few years. I quickly merged into the group with their selfless help.

Finally, I want to thank my parents who are always there for me.

Zhouyuan Li

Contents

List of Tables

List of Figures

Acronyms

MRA	multi-functional reconfigurable antenna
MRAA	multi-functional reconfigurable antenna array
NSGA	non-dominate sorting genetic algorithm
RF	radio frequency
MIMO	multiple input multiple output
AR	axial ratio
EM	electromagnetic
WLAN	wireless local area network
MEMS	micro electro mechanical system
GA	genetic algorithm
DC	direct current
BER	bit error rate
SNR	signal-to-noise ratio

Chapter 1

Introduction

Wireless networks, which have experienced an explosive growth in recent years, must support the rapidly increasing demand for high data rates due to the increasing popularity of smartphones, tablets, netbooks, cloud computing, etc. In this regard, a reliable wireless network with self-organizing and self-optimizing properties providing the required high data rates in a spectrally efficient manner becomes an attractive solution. One of the most important modules of such a network is antenna. Antennas are necessary and critical component in these systems, but sometimes their inability to adapt to changing operating environments can limit their performance. Making antennas reconfigurable so that their behavior can adapt to changing system requirements or environmental conditions can alleviate these restrictions and provide additional levels of functionality for systems.

1.1 Reconfigurable Antenna

Reconfigurability, when used in antenna technology, means the capability to change an individual radiator's fundamental characteristics through electrical, mechanical, or other means. Thus, the radiation properties of the reconfigurable antenna are basically changed by morphing its structure. Reconfigurable antenna could be used as single element or in array fashion to provide additional capabilities that may result in wider frequency bandwidths, more scan volumes, or radiation patterns with more desirable side lobe distributions.

One form of the reconfigurable antenna, MRA (multi-functional reconfigurable antenna) can be used as an important additional degree of freedom in adaptive system parameters [1–6], providing significant capacity gains. These additional gains result from the joint optimization of dynamically reconfigurable antenna properties with adaptive space-time modulation techniques in response to the changes in the propagation environment [7].

1.2 Reconfigurable Antenna Application

There are two general application areas, single-element and array. Single element antennas are frequently implemented in portable wireless devices, such as cellular phone, or laptop. Single antennas typically used in these devices are monopole or microstrip antenna, which may not have frequency or pattern reconfigurability. Some devices may use two or three antennas for diversity reception on small devices to increase the probability of receiving a usable signal, but usually only one of the antennas is used for transmission at a transient time. Reconfigurable antenna in such a situation could provide numerous advantages. For instance, the ability to tune the antenna's operating frequency could be utilized to change operating bands, filter out interfering signals, or tune the antenna for a new environment. If the radiation pattern of an antenna could be changed, the maximum signal power could be directed to the desired position and use less power for transmission, resulting in a significant saving in battery power.

Another application area, antenna array, already has a well established set of limitations [8–12]. For instance, current planar phase array technology is typically limited in both scan angle and frequency bandwidth as a result of the limitations of the individual array elements and the effects of antenna elements spacing. The addition of reconfigurability to array element in the form of reconfigurable antenna can provide additional degrees of freedom that may result in more desirable radiation properties.

There are generally three aims for achieving reconfigurability in antenna:

1) Frequency reconfigurability,

2) Polarization reconfigurability,

3) Radiation pattern reconfigurability.

Different combination of these features can also be achieved know as compound reconfigurability.

1.3 Dissertation Outline

This dissertation consists of seven chapters. Chapter 1 introduces the concept of reconfigurable antenna with emphasis on the description of the advantages of MRA. Chapter 2

describes the latest research progress in literature. Chapter 3 presents the detailed design, fabrication, and measurement of a single element MRA, which provides three beam steering directions by using a parasitic layer in the design. Chapter 4 extends the concept of single element MRA to MRAA (multi-funtional reconfigurable antenna array), and the theory of MRAA operation is developed. To validate the design, prototypes of MRA and MRAA was fabricated with good agreement between simulations and measurements. Chapter 5 takes into account the practical limit of the MRA by developing the MRA operating at IEEE 802.11 b/g band with PIN diode switches. Since 802.11 b/g band is one of the most popular WLAN communication bands, the well-matched simulation vs. measurement indicates that this parasitic layer based MRA have a strong potential for future commercialization. Chapter 6 presents a simplified MRA design compared to that presented in Chapter 5, with a different operating frequency at 5.17-5.83 GHz for IEEE 802.11 ac standard. Since the fractional bandwidth is over 12%, one of the main challenges of this design is that radiation pattern integrity has to be maintained over the whole band. The final measurement results agree well with simulation, thus the design process is validated. Finally, Chapter 7 concludes all of the designs in this dissertation and future work is discussed.

Chapter 2

Literature Review

2.1 Methods for Achieving Frequency Response Reconfigurability

2.1.1 Switches

The effective electrical length the antenna, and thus its operating frequency can be changed by adding or removing part of the antenna length through electrical, optical, mechanical, or other means. Groups have demonstrated different kinds of switching technology, such as optical switches, PIN diodes, FETs, and radio frequency microelectromechanical system (RF-MEMS) switches, in frequency-tunable monopole and dipole antennas for various frequency bands. For instance, Panagamuwa et al. [13] have demonstrated a dipole antenna equipped with two silicon photo-conducting switches, as shown in Fig. 2.1.

Light from infrared laser diodes guided by fiber-optic cables was used to control the switches. With both switches closed, the antenna operated at a lower frequency of 2.16 GHz, and with both switches open, the antenna operated at 3.15 GHz.

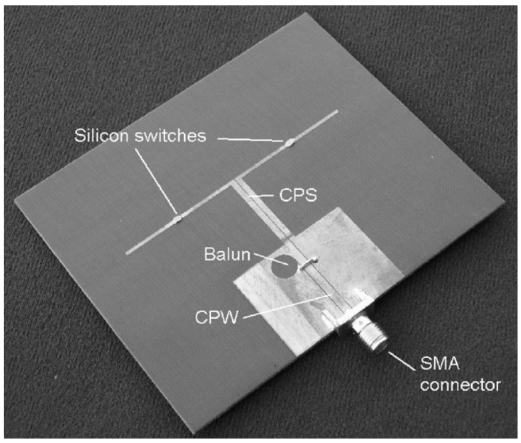

Fig. 2.1: Optically switched dipole antenna providing frequency reconfigurability.

A degree of pattern reconfigurability is also achieved with this design by activating only one switch at a time. However, this pattern reconfiguration comes with a change in operating frequency, which shifts to 2.7 GHz under these conditions [13]. Kiriazi et al. also presented a similar design with antenna length change using RF-MEMES switches [14].

2.1.2 Variable Reactive Loading

Recently, a microstrip patch antenna has been tuned using integrated RF-MEMS capacitors [15]. Shown in Fig. 2.2, the capacitors are implemented on a CPW tuning stub and actuated with continuous DC bias voltages up to 12V, which produces operating frequencies between 15.75 and 16.05 GHz. The unique monolithic approach in the design eliminated the need for plated through hole vias, and the resulting patterns show little effect of the proximity of the tuning stub. Other microstrip antennas with slots equipped with solid-state varactors have also been demonstrated [16].

2.2 Methods for Achieving Polarization Reconfigurability

2.2.1 Fundamental Theory of Operation

The direction of current flow on the antenna translated directly into the polarization of

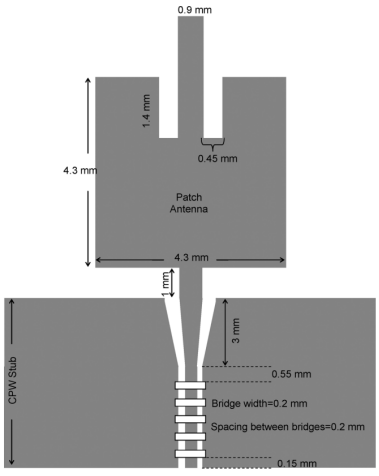

Fig. 2.2: Frequency-tunable microstrip patch antenna with RF-MEMS capacitors and CPW tuning stub.

the electrical field in the far field of the antenna. To achieve polarization reconfigurability, the antenna structure, material properties, and/or feed configuration have to change in ways that alter the direction of current flows on the antenna. Polarization reconfigurations can take place between different kinds of linear polarization, between right- and left-handed circular polarizations, or between linear and circular polarizations. The mechanisms to achieve these reconfigurabilities (e.g., switches, structural changes) are generally the same as those described for frequency reconfigurability earlier, although their implementations may be different. The main difficulty of this kind of reconfigurability is that it must be accomplished without significant changes in impedance or frequency characteristics.

2.2.2 Switches

Slot antennas, such as the one developed by Fries et al. [17], have been implemented to deliver polarization reconfigurability. Fries et al. describe a slot-ring antenna equipped with PIN diodes to reconfigure between linear and circular polarization or between two circular polarizations [17].

Figure 2.3 shows the basic topology of the antenna, where Fig. 2.4 depicts the specific diode positions, biasing, and ground plane configurations for two designs. For the linear-circular design Fig. 2.4 (a), forward biasing the diodes across the small discontinuities at 45^o and -135^o relative to the feed point delivers linear polarization, while reverse biasing the diodes results in circular polarization. The design in Fig. 2.4 (b) includes additional symmetric discontinuities to support switching between left- and right-handed circular polarizations.

In both designs, the ground planes are carefully designed to support proper DC biasing for the diodes while providing RF continuity through capacitors connected between ground plane sections. This radiating structure is a good example of the additional factors that must be taken into account when transforming from a fixed antenna to a reconfigurable antenna: the fundamental structure may stay the same, but critical adjustments are required to enable both proper DC biasing and RF performance.

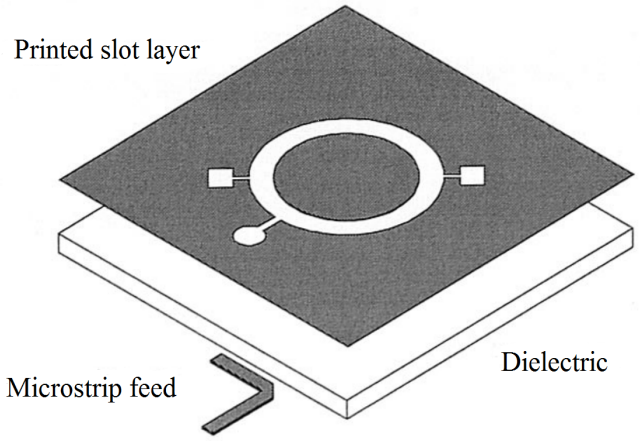

Fig. 2.3: Basic topology of a microstrip-fed circularly polarized slot ring antenna.

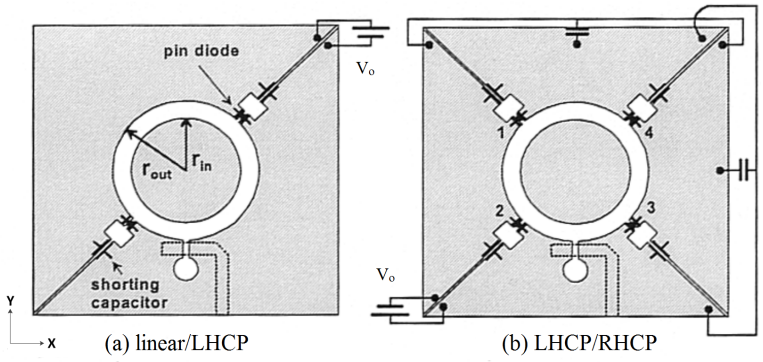

Fig. 2.4: Two polarization-reconfigurable slot ring antennas: (a) switchable between linear and left-hand circular polarization, (b) switchable between left- and right-hand circular polarization.

2.2.3 Material Changes

Rainville and Harackiewicz [18] presented a polarization-tunable microstrip antenna based on static magnetic biasing of a ferrite film. As with microstrip antenna on bulk ferrite substrates [19–21], the co-polarized fields are much less dominant than those from a traditional microstrip patch antenna. Rainville and Harackiewicz [18] took advantage of the fact that the applied static bias field tuned the frequency of the cross-polarized field to create a range of elliptical polarizations. Optimization of feed point and ferrite film properties could result in purely circular and linear polarizations as well.

2.3 Methods for Achieving Radiation Pattern Reconfigurability

2.3.1 Fundamental Theory of Operation

The arrangement of currents on an antenna structure directly determines the spatial distribution of radiation from the structure. This relationship between the source currents and the resulting radiation makes pattern reconfigurability without significant changes in operating frequency difficult. To develop antennas with specific reconfigurable radiation patterns, a designer must determine what kinds of source current distributions, including both magnitude and phase information, are relevant. Once a topology for the current distribution is determined, a base antenna design can be selected and then altered to achieve the desired source current distribution. This design process is very similar to that of array synthesis. The following task is to either arrange the design so that the frequency characteristics are unchanged or to compensate for changes in impedance with tunable matching circuits at the antenna terminals. In some cases, antenna types such as reflector antennas or parasitically coupled antennas are selected so that the driven part is more isolated from the reconfigured portion of the structure, allowing the frequency characteristics to remain relatively unchanged while radiation patterns are reconfigured.

It should be noted that some antennas have been developed to deliver multiple radiation patterns at a single frequency point through careful design of feed structures to couple degenerate modes that possess different radiation patterns [22]. Although these kinds of

designs do not strictly meet the definition of reconfigurability described above, they do provide insight for a general approach to develop such designs.

2.3.2 Mechanical Change

With the reflective surface physically isolated from the primary feed, reflector antennas are a natural choice for applications that require radiation pattern reconfigurability independent of frequency. Changes in an effective reflector have been demonstrated using reconfigurable high-impedance surfaces [23]. A lattice of small resonant elements produces high-surface impedance near their resonant frequency, creating in effect an artificial ground plane. Changing the capacitance between resonant elements across the lattice through mechanical means creates a phase gradient that can produce a steered beam when the lattice is used as a reflector [24].

A closely related approach has also been used to develop a reconfigurable leaky-wave antenna using mechanical tuning [25]. In this case, a horizontally polarized antenna is used to couple energy into leaky transverse electric waves on a tunable impedance surface. A diagram of the high impedance surface and the moveable top capacitance surface, is shown is Fig. 2.5. The radiated beam from the surface can be steered in elevation over a range of 45^o by changing the capacitance of the surface through mechanically shifting the top capacitive plane.

The horizontally polarized antenna and impedance surface are shown in Fig. 2.6. An electronically tuned version of this antenna that uses varactors can produce reconfigurable backward as well as forward leaky-wave beams [26, 27].

2.3.3 Parasitic Tuning

One of the most effective methods to change radiation patterns independently from frequency behavior is to use electrically tuned or switched parasitic elements. This method has several attractive qualities: isolation of the driven elements from the tuned element; potentially wide frequency bandwidth. Fundamentally, tuning of antenna radiation patterns in this manner relies on the mutual coupling between closely spaced driven and parasitic

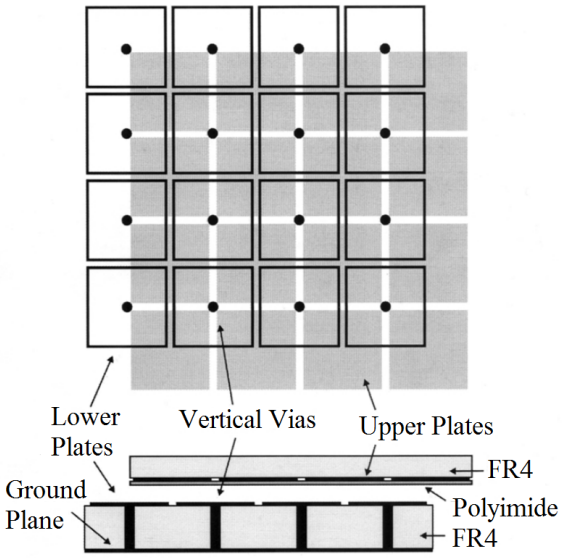

Fig. 2.5: Mechanically reconfigurable impedance surface consisting of two printed circuit boards: a high-impedance ground plane and a separate tuning layer. The tuning layer is moved across the stationary high-impedance surface to vary the capacitance between the overlapping plates and tune the resonance frequency of the surface.

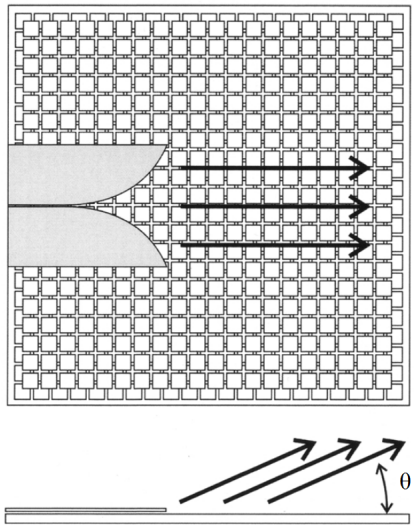

Fig. 2.6: A horizontally polarized antenna couples energy into leaky modes on the tunable impedance surface. The waves propagate across the surface and radiate at an angle governed by the surface resonance frequency with respect to the excitation frequency. By tuning the surface resonance frequency, the beam is steered in the elevation plane.

elements, resulting in effective array behavior from a single feed point. Therefore, reconfigurability in radiation patterns are achieved through changes in the mutual coupling between the elements, which, in turn, changes the effective surface currents on both the driven and parasitic elements.

In 1978, Harrington proposed a parasitic dipole array that continues to see applications today in various related forms [28]. Figure 2.7 shows the driven dipole element surrounded by parasitic dipoles loaded with tunable reactance. Variations in the load reactance of each parasitic element change the magnitude and phase of the signal on each array element, resulting in a directive beam in a desired direction.

Another form of antenna with both frequency and polarization reconfigurability [1] is shown in Fig. 2.8. The antenna is composed of a large amount of metallic pixels connected together by switches. This conceptual antenna provides 10 different reconfigurable modes of operation corresponding to the combination of two operating frequencies (4.1 and 6.5 GHz) and five reconfigurable polarizations of the radiated field (linear X, linear Y, dual linear, right hand circular, and left hand circular).

This multi-metallic pixel architecture can also be employed as a parasitic surface to achieve reconfigurability of radiation patterns. The details of the designs will be given in the following chapters.

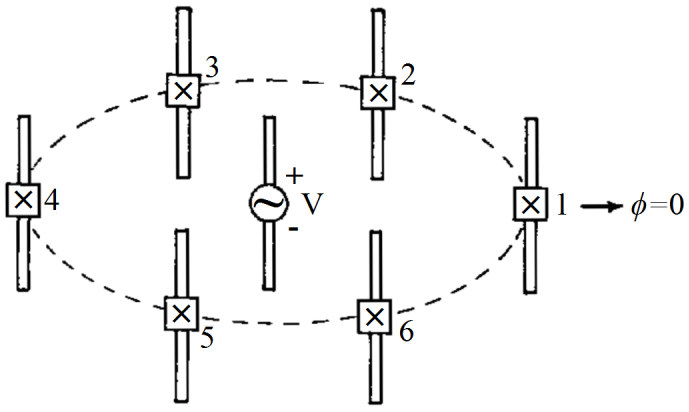

Fig. 2.7: A seven-element circular array of reactive loaded parasitic dipoles for reconfigurable beam steering.

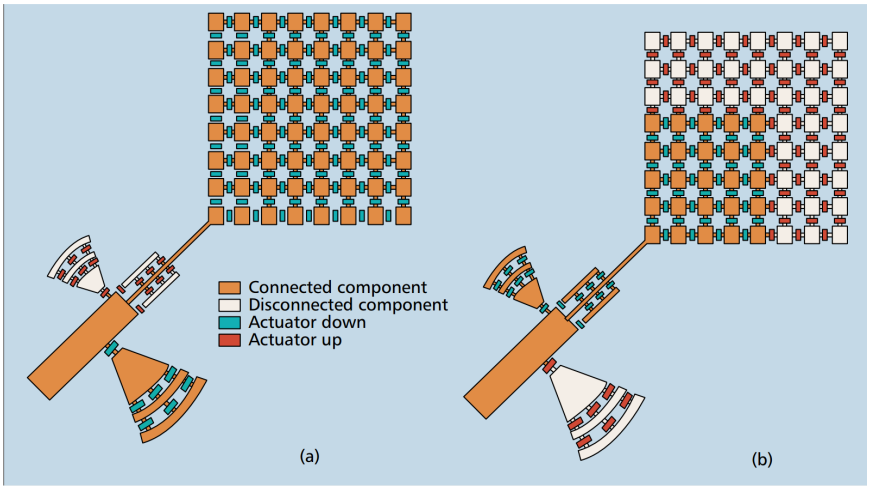

Fig. 2.8: Different configurations for different modes of operation.

Chapter 3

MRA with Beam-Steering Capabilities

3.1 Introduction

A beam-steering antenna based on a parasitic layer operating at around 5.6 GHz is presented [29, 30]. It is capable of steering its beam into three directions ($\theta = -30^o, 0^o, 30^o$). The structure consists of a driven microstrip-fed patch element and a parasitic layer located on top of the driven patch. The upper surface of the parasitic layer has a grid of 5×5 electrically-small rectangular-shaped metallic pixels, which can be connected/disconnected by means of switching, thus the parasitic pixel surface geometry is changed. The electromagnetic mutual coupling between the driven patch and the parasitic pixel surface is responsible to achieve the desired beam-steering. The prototypes of the designed antennas have been fabricated showing ∼8 dB realized-gain in all steered beam directions.

Multi-functional reconfigurable antennas (MRAs) with dynamically changeable antenna properties in frequency, radiation pattern and polarization have recently gained significant interest [31,32]. A typical MRA structure consists of a number of metallic segments of various geometries along with a switching circuitry. The switching circuitry is used to connect/disconnect the metallic segments, thereby changing the current distribution on the antenna, which in turn changes the antenna properties. Majority of the MRAs presented so far [31,33] integrate the switching network along with the associated control circuitry within the driven antenna region. However, for a MRA with large number of reconfigurable modes of operation, the switching network becomes very complex, which may severely degrade the antenna performance due to deleterious coupling effects.

In this chapter, a new reconfiguration technique is presented, where the switching network is separated from the driven patch element [34]. As shown in Fig. 3.1, the switching network lies on the upper surface of the parasitic layer (which contains 5×5 rectangular-

shaped metallic pixels); thereby it is separated from the driven element. This reconfiguration approach provides significant advantages: 1) Since switches are separated from the driven antenna, they get exposed to only a minor portion of the RF power available on the driven antenna, which prevents switch failures (due to limited power handling capability of the switches). 2) As the switching control circuitry is separated from driven antenna element, it can be designed separately to meet the overall system performance requirements. Also, deleterious coupling effects that may otherwise disturb the antenna performance are minimized due to the separation. 3) The fabrication of the antenna becomes easier as the switching network can be fabricated separately. It can then simply be assembled together with the driven antenna. It is also worth noting that, with the presented technique, there is no constraint on the distance from driven antenna to the parasitic pixel surface, which is simply chosen to be the thickness of Integrated Circuit (IC) compatible quartz substrate (0.525mm). In contrast to the typical distance of $\sim \lambda/4$ for the previous work on antennas with parasitic elements [28], this design is more compact.

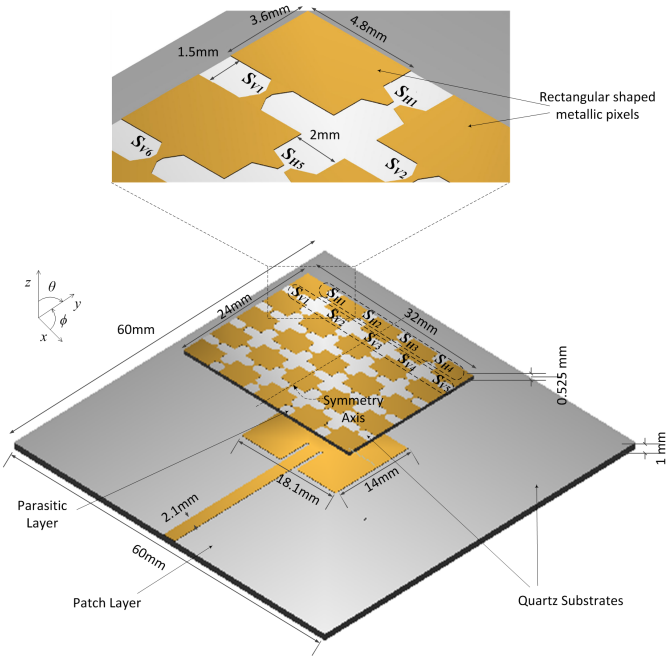

Fig. 3.1: 3-D Schematic of the beam-steering antenna with a magnified view of adjacent pixels (For the sake of illustration, the parasitic layer is shown to be suspended on top of the patch layer).

3.2 Antenna Architecture and Working Mechanism

The 3-D schematic of the beam-steering antenna with critical design parameters is shown in Fig. 3.1. It consists of two layers, namely patch and parasitic layers. The patch layer ($60 \times 60 \times 1\ mm^3$), which is built on a quartz substrate ($\epsilon_r = 3.9$, $\tan\delta = 0.0002$ at $f = 10$ GHz) [35], contains the driven patch antenna element and microstrip feed line. The choice of quartz substrate is due to its good RF properties and IC process compatibility. The standard driven patch antenna is designed to operate at ∼5.6 GHz and is fed by a microstrip feed line of 50 characteristic impedance. The parasitic layer ($32 \times 24 \times 0.525\ mm^3$) is placed on top of the patch layer. The upper surface of the parasitic layer has a grid of 5×5 rectangular-shaped metallic pixels with individual pixel size being $4.8 \times 3.6\ mm^2$. The geometry of this parasitic pixel surface can be changed by turning ON or OFF the switches between adjacent pixels, which in turn changes the current distribution of the antenna, resulting in different antenna properties. The switches used here are the series type DC contact MEMS switches. Notice that in this work, for simplicity, the interconnecting switches between adjacent pixels are replaced by perfect short circuit (ON) or perfect open circuit (OFF) as shown in the inset of Fig. 3.1. The horizontal and vertical groups of switches shown in Fig. 3.1 are numbered in order from the top left corner to the bottom right corner of the parasitic pixel surface, which are accordingly labeled as S_{Hi} (i = 1, 2, ... 20) and S_{Vi} (i = 1, 2, ... 20), respectively. The vertical distance from the patch antenna element to the pixel surface is 0.525mm, which is determined by the substrate thickness of the parasitic layer. The substrate for the parasitic layer is also chosen to be quartz.

The working mechanism of the presented antenna can simply be explained by the theory of reactively controlled directive arrays [28], where the antenna system is composed of one driven antenna and multiple parasitic elements. It is shown that the antenna radiation characteristics are controlled by properly changing the reactive loads among parasitic elements and the driven element. By using network analysis, these reactive loads can be described by mutual impedance with every element being assigned a port. Note

that in the presented antenna, the mutual impedances, or equivalently reactive loads, are varied by changing the shapes and relative locations of the parasitic elements (by connecting/disconnecting adjacent pixels), which eventually results in three different beam-steering angles ($\theta = -30^o, 0^o, 30^o$). The mutual impedance between the ports of element i and element j is defined as

$$Z_{ij} = \frac{V_i}{I_j}_{I_i=0, i\neq j}, \tag{3.1}$$

where V_i is the voltage applied to the port of element i and I_j is the current induced on the element j when all the ports but jth port are open circuited. If the applied voltages (V_i) and mutual impedances are known for a given beam-steering angle of θ, the current in each parasitic element can be calculated resulting in the total radiated E-field, which can be expressed as follows:

$$E_{tot,m} = \sum_{i,m} E(I_{i,m}), m = 1, 2, 3 \ldots, \tag{3.2}$$

where integer m represents each mode of operation ($\theta = -30^o, 0^o, 30^o$), and $E(I_{i,m})$ is the field produced by current $I_{i,m}$. Although $\theta = -30^o, 0^o, 30^o$ are the targeted directions, discrete steering angles such as $5^o, 10^o$ or 15^o can also be obtained using MEMS switches, which interconnect the pixels on the upper surface of the parasitic layer. Moreover, varactor diodes can be used instead of MEMS switches for continuous beam scanning applications.

Given the symmetric feature of the parasitic layer (see Fig. 3.1) once the configuration with steering angle θ has been obtained, the corresponding configuration of $-\theta$ can simply be found by mirroring the switch status along the symmetry axis shown in Fig. 3.1.

3.3 Optimization Methodology

In the presented antenna, there exist a large number of interconnections among 5×5 rectangular shaped metallic pixels of the parasitic layer. Therefore a multi-objective genetic algorithm (GA) optimization is employed in conjunction with full-wave analysis to

determine the switch statuses that result in two aims: 1) required realized gain in three directions of arrival, ($\theta = -30^o, 0^o, 30^o$); 2) desired frequency bandwidth (BW) of $\sim 3\%$ at $\sim$5.6 GHz. The multi-objective GA is different from single-objective GA in the sense that, it has more than one aim which conflict each other and should be evaluated simultaneously. Although, many different algorithms have thus far been proposed in solving multi-objective problems, non-dominated sorting genetic algorithm (NSGA) has been one of the most popular, which has an efficient sorting algorithm and incorporates elitism. An improved version of this algorithm is NSGA-II [36], which is used in this work. To perform full-wave analyses, ANSYS HFSS [37] is used. The optimized simulation results along with their measurements are discussed in the next section.

3.4 Fabrication and Measurements

To validate the theoretical analyses of the beam-steering antenna, three prototypes each of which corresponding to one of the beam steering angle ($\theta = -30^o, 0^o, 30^o$) have been designed and fabricated. The radiation and impedance characteristics of these prototypes have been measured and compared with those of the simulated results. The parasitic and the driven patch antenna layers were fabricated separately, which were then bonded together to obtain the prototypes. Gold (Au) metal (conductivity: $\sigma = 4.098 \times 10^7$ S/m) is deposited on quartz substrates by an electron beam deposition and chemically etched in a clean room to form the patch antennas and the pixels of the parasitic layer.

The prototypes were designed to operate at around 5.6 GHz. Figure 3.2 shows the measured and simulated reflection coefficients corresponding to the beam-steering modes: $\theta = 30^o$ and $\theta = 0^o$ along with their switch statuses. Please note that in all three modes of operation ($\theta = -30^o, 0^o, 30^o$) the switches labeled S_{Hi} (i=9, 12, 13, 16) and S_{Vi} (i=1,3,5,18) are always ON while the switches S_{Hi} (i=1,4) and S_{Vi} (i=7,9,13,16) are always OFF. The switch statuses for $\theta = -30^o$ mode can be obtained by performing an inverse operation on the switch statuses of $\theta = 30^o$ mode due to the symmetry of the parasitic pixel surface. Notice that the reflection coefficient is only shown for one of the two symmetric beam-steering angles ($\theta = 30^o$) as the results for $\theta = -30^o$ is identical due to the symmetry

feature of the parasitic pixel surface as explained above. As is seen from Fig. 3.2, the simulated and measured results agree reasonably well, having a common BW around 5.65 GHz as highlighted in this figure. Figure 3.3 (a) and (b) show the radiation patterns at the resonant frequency of interest (∼5.65 GHz) of all beam-steering prototypes ($\theta = -30^o, 0^o, 30^o$), respectively. The simulated and measured results agree well indicating that the realized gain values are above 8 dB for all beam-steering angles.

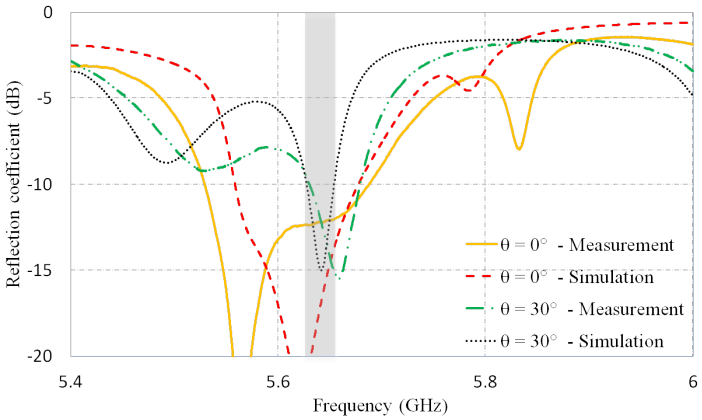

θ = 0⁰	$S_{Hi}(i = 2, 8, 11, 14, 17, 19) = S_{Vi}(i = 2, 8, 10, 15, 17)$ = OFF
	$S_{Hi}(i = 3, 5, 6, 7, 10, 15, 18, 20) = S_{Vi}(i = 4, 6, 11, 12, 14, 19, 20)$ = ON
θ = 30⁰	$S_{Hi}(i = 2, 6, 8, 11, 14, 17, 19) = S_{Vi}(i = 2, 8, 10, 11, 14, 19)$ = OFF
	$S_{Hi}(i = 3, 5, 7, 10, 15, 18, 20) = S_{Vi}(i = 4, 6, 12, 15, 17, 20)$ = ON

Fig. 3.2: Measured and simulated reflection coefficients of the prototypes for beam steering angles $\theta = 30^o$ and $\theta = 0^o$ along with their switch statuses.

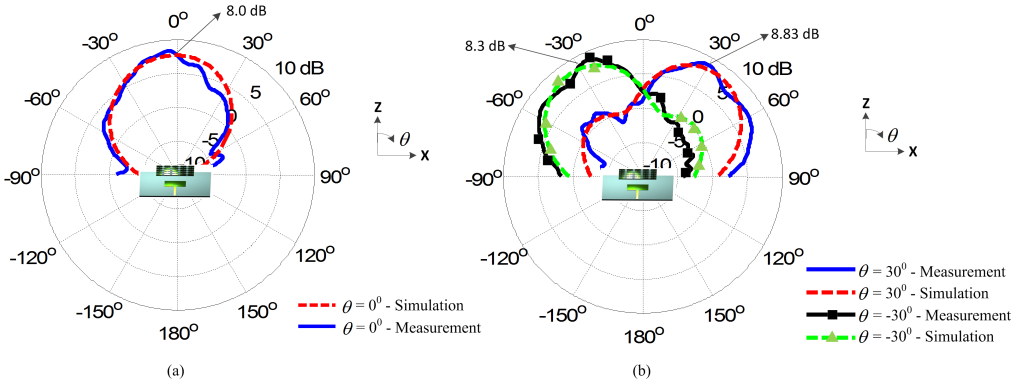

Fig. 3.3: Measured and simulated realized gain patterns of the beam-steering antenna prototypes for (a)$\theta = 0^o$, (b) $\theta = -30^o, 30^o$. The patterns are cut in the x-z plane at the center frequency (5.65 GHz) of the common frequency band as highlighted in Fig. 3.2.

3.5 Conclusions

A beam-steering antenna based on a parasitic layer which can steer its beam into three different directions ($\theta = -30^o, 0^o, 30^o$) was introduced in this chapter. The presented antenna provides significant advantages both in terms of design and manufacturing as the driven antenna and the parasitic layers are separated from each other. An efficient design methodology which combines multi-objective genetic algorithm and full-wave analyses was employed in determining the switch statuses associated with each beam direction. Prototype antennas were designed, fabricated, and measured. The results from measurements and simulations agreed reasonably well indicating that the presented antenna can achieve $\sim$8 dB realized gain for all the beam-steering angles. The results of this work can provide significant guidance for multi-functional reconfigurable antenna designers.

Chapter 4

A New Class of Antenna Array with a Reconfigurable Element Factor

4.1 Introduction

Wireless networks, which have experienced an explosive growth in recent years, must support the rapidly increasing demand for high data rates due to the increasing popularity of smartphones, tablets, netbooks, cloud computing, etc. In this regard, a reliable wireless network with self-organizing and self-optimizing properties providing the required high data rates in a spectrally efficient manner becomes an attractive solution. One of the most important modules of such a network is a high-gain intelligent antenna array, which is capable of steering its beam toward desired directions, while simultaneously placing nulls toward undesired directions of interferers, and thereby maximizing the signal-to-noise ratio of the desired signal. A phased array antenna (PAA) [8–12] can accomplish these tasks at the cost of increased size, complexity and high price, which are, most of the time, prohibitive for commercial wireless networks.

In meeting the desired performance characteristics of existing and future wireless networks without compromising the size and cost of the system, multi-functional reconfigurable antennas (MRAs) have gained a significant interest during the last several years [1, 2, 6, 31, 38]. An MRA is a single antenna element, which is capable of providing dynamically changeable antenna properties in frequency, radiation pattern and polarization by morphing its architecture. The combination of multiple individual MRAs can be arranged in an array fashion forming a multi-functional reconfigurable antenna array (MRAA). The MRAs with variable properties being the individual radiators of the MRAA constitutes the main difference with a standard linear antenna array, which consists of radiators of which

properties are fixed by the initial design and cannot be changed. A standard array has a fixed element factor and its radiation pattern is solely controlled by the array factor, which is determined by the geometrical position of the radiators forming the array and their excitations. On the other hand, MRAA has a variable element factor [39, 40], which presents a significant additional degree of freedom in providing highly agile array properties in frequency, polarization and radiation pattern as compared to a standard antenna array.

In this chapter, a linear array composed of equally spaced four identical MRAs, i.e., 4×1 MRAA is presented. Each individual MRA consists of an aperture-coupled fed patch antenna with a parasitic layer placed above it (see Fig. 4.1) [30, 34].

The architecture of this MRA is different than that of inset-fed microstrip MRA [29,30], providing broader bandwidth and enhanced beam steering capabilities with higher gain. Each individual radiator of the MRAA is capable of producing eight modes of operation by configuring the surface geometry of the parasitic layer, where the 4×4 electrically small rectangular-shaped metallic pixels (*parasitic pixel surface*) can be connected/disconnected by means of switching. The modes of operations are the three steerable beam directions (θ_{xz}= -30^o, 0^o, 30^o) with circular and linear polarizations in the *x*-*z* plane and another two steerable beam directions ($\theta_{yz} = -30^o, 30^o$) in the *y*-*z* plane with linear polarization at the frequency range of 5.4-5.6 GHz. Full-wave analysis by HFSS [37] and multi-objective genetic algorithm optimization are jointly employed to determine the interconnecting switches' status (i.e., short or open circuit) corresponding to the eight modes of operation.

The advantages of MRAA as compared to a conventional liner array can be summarized as follows: 1) While a conventional linear array is limited to steer its main beam only in the plane (*y*-*z* plane in this work), which contains the line (*y*-axis in this work) on which the centers of the array elements lie, the presented MRAA can perform beam steering both in the *x*-*z* and *y*-*z* planes. 2) For MRAA, the beam steering in the *x*-*z* plane is achieved by the variable element factor without needing to employ phase shifters. Therefore, the problems such as scan loss and beam-squint associated with the progressive phase shift between array elements are alleviated. 3) When the beam is steered in the *y*-*z* plane, MRAA takes

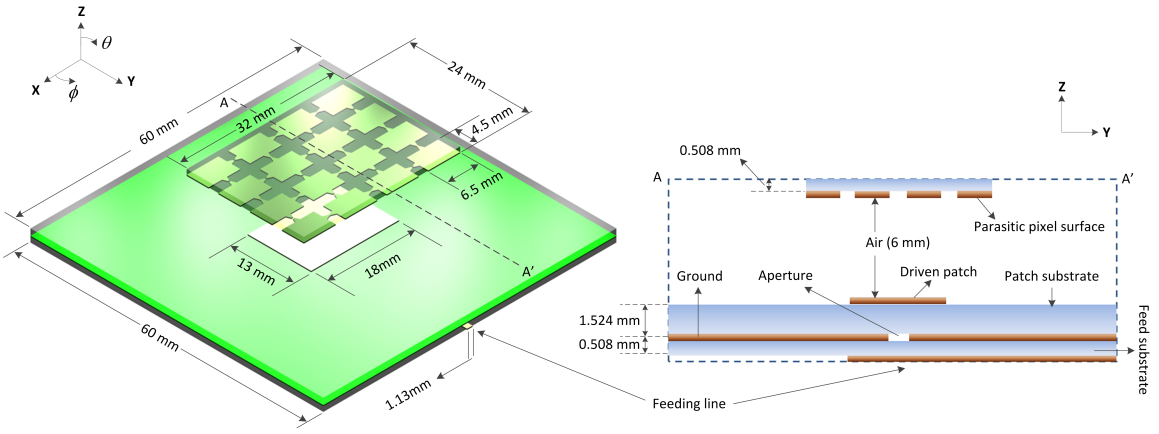

Fig. 4.1: 3-D schematic and the cross section view of an individual element of the MRAA (MRA).

advantage of optimizing the variable element factor in conjunction with array factor. The main beam direction of each individual radiator is aligned with the maximum of the array factor, thereby a significant increase in array gain is accomplished. 4) Each radiator of a MRAA has a higher gain (∼2 dB) than that of conventional array resulting further increase in the array gain. 5) For the conventional array to achieve polarization reconfigurability, additional feed network including power dividers or hybrids needs to be introduced. For MRAA this can be readily accomplished as the individual radiators can change the sense of polarization from linear to circular. These advantages of an MRAA can be used to enhance the capabilities of the $IEEE$ 802.11a, b, g, n, and ac systems. In particular, $IEEE$ 802.11n and $IEEE$ 802.11ac MIMO systems equipped with MRAA can provide significant performance improvement over a MIMO system employing single-function antennas [6].

4.2 MRAA Structure and Working Mechanism

4.2.1 Individual MRA Element of the MRAA

Structure and Working Mechanism: The 3-D schematic and cross section view of the individual element of the MRAA, i.e., MRA, are depicted in Fig. 4.1. This MRA uses an air substrate for the parasitic layer and aperture-coupled feed mechanism as opposed to

microstrip inset feed to achieve improved performances as compared to the MRA presented in Chapter 3 [29, 30]. Its geometry is symmetric along x- and y- axes, which simplifies the optimization procedure of determining the modes of operation. The main two components of the MRA architecture are, namely, the driven patch antenna and parasitic layer. The driven patch (18×13 mm^2) is designed to operate at ~5.4 GHz and fed by a 50-Ohm microstrip line through an aperture (7×0.7 mm^2) etched on the center of the common ground plane. The feed layer ($60 \times 60 \times 0.508$ mm^3) and the patch layer ($60 \times 60 \times 1.524$ mm^2) are built respectively by using the substrate, RO4003C ($\varepsilon_r = 3.55, \tan\delta = 0.0021$). The same substrate ($32 \times 24 \times 0.508$ mm^3) is also used to form the reconfigurable parasitic surface, which consists of 4×4 rectangular-shaped metallic pixels with individual pixel size being (6.5×4.5 mm^2). The electrical properties of the parasitic layer, however, are determined by the $6mm$ thick air layer, where the main role of the RO4003C substrate is to provide mechanical support for the pixels. The $6mm$ thickness of this layer has been determined to be optimum in terms of the trade-off among the performance parameters of bandwidth, gain, and beam-tilt capability. The substrate material used for this air layer is polymethacrylimide foam with $\varepsilon_r = 1.043$ and $\tan\delta = 0.0002$ at 5 GHz [41].

The working mechanism of an antenna system, which is composed of one driven antenna and multiple parasitic elements, might be described by the theory of reactively controlled directive arrays developed by Harrington [28]. It was shown that the main beam direction of the driven antenna can be directed into a desired direction by the proper reactive loading of the parasitic elements. In the presented MRA, the proper reactive loading corresponds to a specific geometry of the parasitic pixel surface, which is obtained by switching on and off (connecting/disconnecting) the adjacent pixels of this surface. Notice that, for simplicity, the switch connections are used as perfect short and perfect open in this work. This MRA is not only capable of steering its main beam but can also change the polarization state from linear to circular for a given beam direction. The eight modes of operation are the three steerable beam directions (θ_{xz}= -30^o, 0^o, 30^o) with linear and circular polarizations in the x-z plane and two steerable beam directions ($\theta_{yz} = -30^o, 30^o$) in the y-z plane with linear

polarization. Figure 4.2 illustrates the planes in which the beam is steered, the definitions of the beam-steering angles (θ_{xz} and θ_{yz}) and the placement of the MRA geometry, which is symmetric along x- and y-axes.

MRA: Simulation and Measurement Results: Multi-objective genetic algorithm in conjunction with full-wave EM analysis has been employed to determine the parasitic pixel surface configurations, which is to find the status (open or short circuit) of the interconnections between adjacent pixels. The details of the multi-objective genetic algorithm optimization technique [30] are omitted in this chapter.

The optimized geometries of the parasitic pixel surface with interconnection configurations corresponding to each of the eight different modes of operation are shown in Fig. 4.3. Notice that the configurations of the $\theta_{xz} = -30^o$ and $\theta_{yz} = -30^o$ are symmetric with those of the $\theta_{xz} = 30^o$ and $\theta_{yz} = 30^o$ modes, along y- and x-axes, respectively. This is due to the symmetric architecture of the MRA, along x- and y- axes.

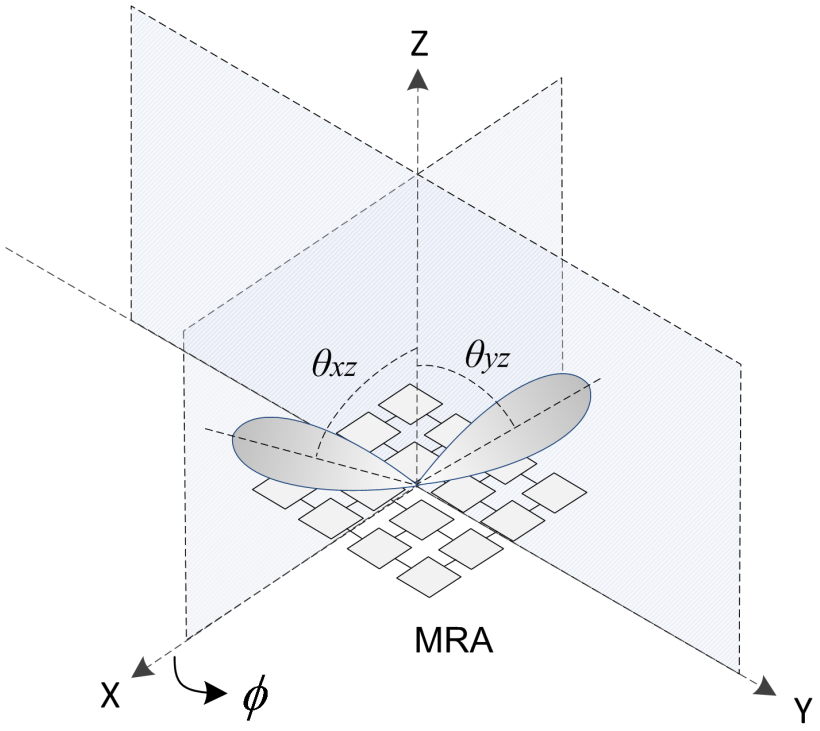

Fig. 4.2: The beam-steering capabilities of an MRA in the $x-z$ ($\theta_{xz} = -30^o, 0^o, 30^o$) and $y-z$ planes ($\theta_{yz} = -30^o, 30^o$). The MRA structure is symmetric along $x-$ and $y-$ axes.

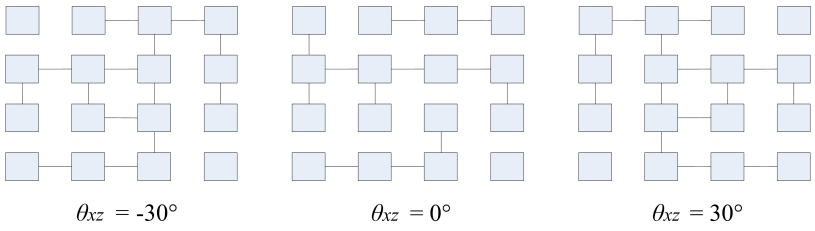

(a) Beam steering modes in the $x - z$ plane with linear polarization

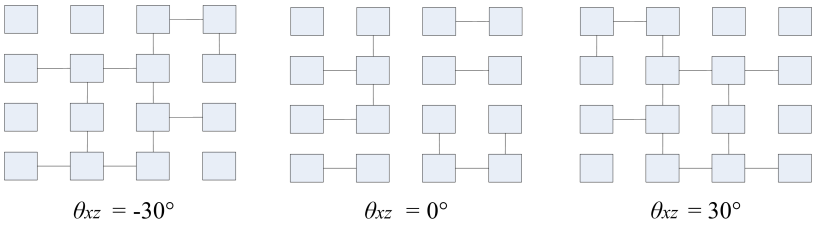

(b) Beam steering modes in the $x - z$ plane with circular polarization

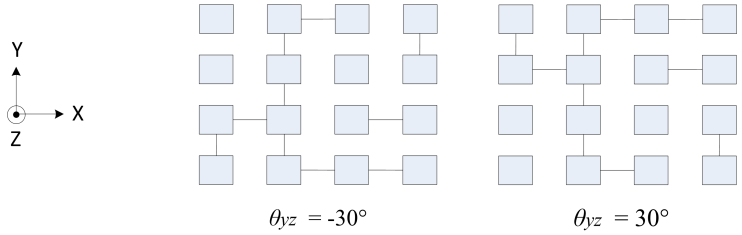

(c) Beam steering modes in the $y - z$ plane with linear polarization

Fig. 4.3: The optimized parasitic pixel surface configurations corresponding to the eight modes of operation produced by an individual MRA.

Five different designs have been chosen and fabricated as prototypes by using standard printed circuit board fabrication techniques. They were measured to validate the results obtained by the theoretical analyses, genetic algorithm optimizations and simulations. These prototypes generate the following modes of operations: the three steerable beam directions ($\theta_{xz} = -30^o, 0^o, 30^o$) in the x-z plane and two steerable beam directions ($\theta_{yz} = -30^o, 30^o$) in the y-z plane with linear polarizations. The reflection coefficients and the radiation patterns in terms of realized total gain have been measured.

Figure 4.4 (a) and (b) show the simulated and measured reflection coefficients for $\theta_{xz} = 0^o$ and 30^o, and $\theta_{yz} = 30^o$ modes of operation with a common bandwidth of ∼150 MHz around the center frequency of 5.5 GHz. There is a good agreement between simulated and measured results indicating a robust MRA design and fabrication procedures. Notice

that the reflection coefficients are only shown for one of the two symmetric beam-steering angles ($\theta = 30^o$) as the results for ($\theta = -30^o$) are identical due to the symmetry feature of the MRA geometry.

Figures 4.5, 4.6, and 4.7 show the simulated and measured realized total gain patterns corresponding to the beam steering angles of $\theta_{xz} = 30^o$ and $\theta_{xz} = -30^o$, $\theta_{xz} = 0^o$, and $\theta_{yz} = 30^o$ and $\theta_{yz} = -30^o$ at the resonant frequency of 5.5 GHz, respectively. The simulated and measured results agree well indicating that the realized maximum gain values are 9.1 $\pm$ 0.1 dB for all modes of operations. It is worth noting the MRA does not only achieve beam steering but also an approximately 2 dB improvement in gain as compared to a standard

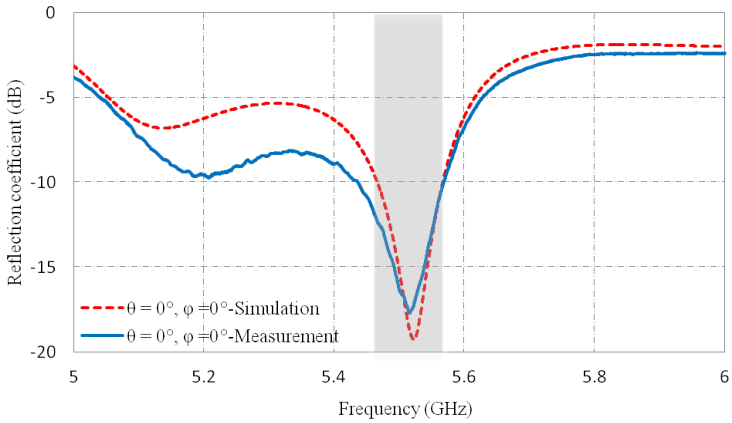

(a)

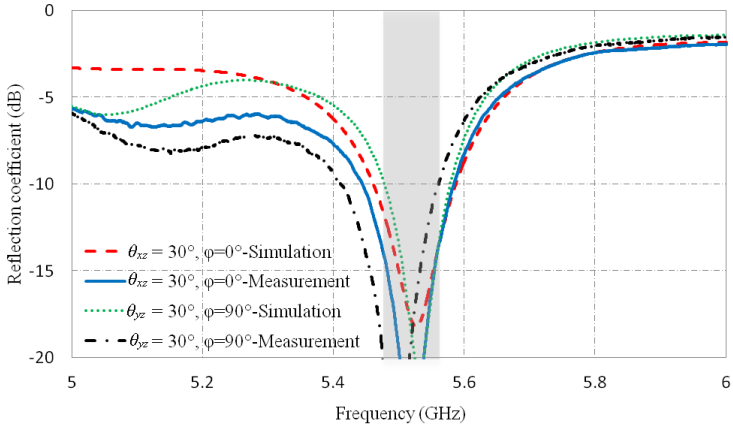

(b)

Fig. 4.4: (a) Simulated, and (b) measured reflection coefficients for MRA prototypes.

patch antenna. The simulation results also show that the modes of operation corresponding to $\theta_{xz} = 30^o$, $\theta_{xz} = -30^o$, and $\theta_{xz} = 0^o$ with circular polarization have gain values of 8.5 $\pm$ 0.2 dB at 5.5 GHz. The reflection coefficients lie within the same common bandwidth shown in Fig. 4.4. The simulated axial ratios for the maximum gain directions with respect to frequency with a common 3-dB axial ratio bandwidth of 100 MHz are shown in Fig. 4.8. Notice that this MRA achieves improved performances compared to the MRA presented in Chapter 3 [29, 30] in all aspects: The bandwidth is improved from $\sim 1\%$ to $\sim 3\%$, and the gain is 9 dB which is 1 dB higher. Also, the presents MRA performs beam steering not only in x-z plane but also in y-z plane, while the previous MRAs beam steering capability is limited to x-z plane only.

4.2.2 MRAA Structure and Design

As investigated in the previous section, the individual radiators of the MRAA have been designed and optimized by using a multi-objective genetic algorithm in conjunction with full-wave analyses, to generate the eight modes of operation within a common operational

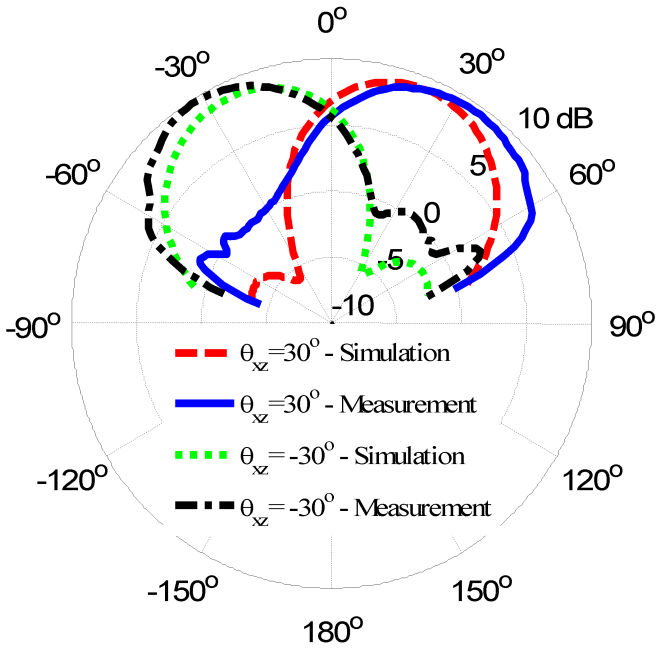

Fig. 4.5: Simulated and measured realized total gain patterns of the individual MRA prototypes for $\theta_{xz} = 30^o$ and $\theta_{xz} = -30^o$.

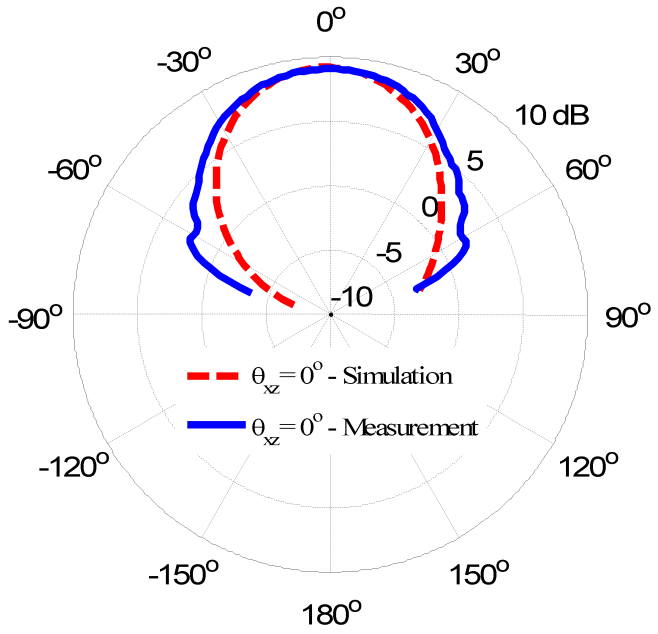

Fig. 4.6: Simulated and measured realized total gain patterns of the individual MRA prototypes for $\theta_{xz} = 0^o$.

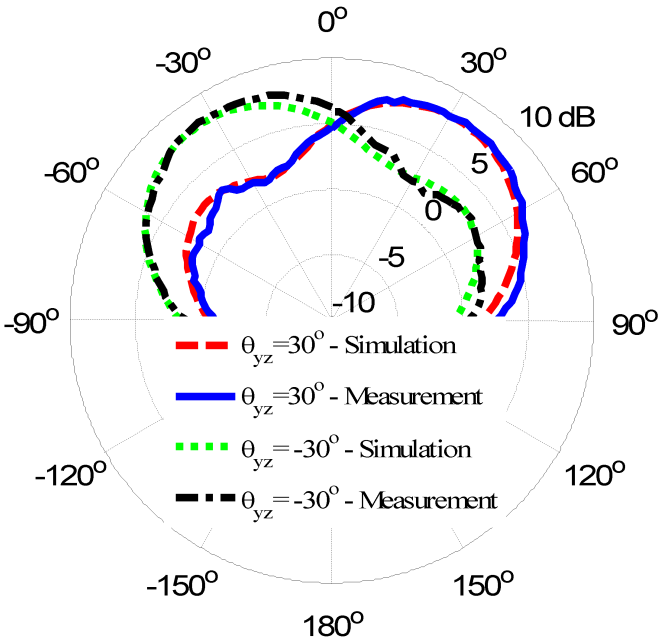

Fig. 4.7: Simulated and measured realized total gain patterns of the individual MRA prototypes for $\theta_{yz} = 30^o$ and $\theta_{yz} = -30^o$.

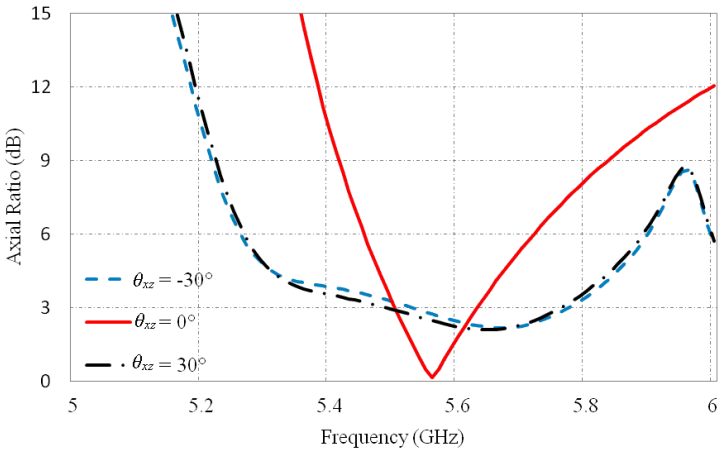

Fig. 4.8: Axial ratios of circular polarization modes versus frequency.

bandwidth with the central frequency of ∼5.5 GHz. The MRAA is then simply formed by the linear combination of four (4×1) identical optimized MRA elements arranged along the y-axis. A 3-D schematic of the MRAA is shown in Fig. 4.9. It is fed by a parallel feed network. The inter-element spacing between the centers of the adjacent radiators is 30 mm, which is approximately half a wavelength at the central frequency of 5.5 GHz. The structures of the feed network, driven patches, and parasitic pixel surfaces are separately formed on RO4003C substrates. The dimensions of the feed network and driven patch structures are $(120 \times 66 \times 0.508\ mm^3)$ and $(120 \times 66 \times 1.524\ mm^3)$, respectively. The 0.508 mm thick parasitic pixel layer has an alternating width between 32 mm and 2 mm and alternating length between 24 mm and 6 mm, thus adjacent parasitic pixel surfaces are connected by $2 \times 6\ mm^2$ strips, as shown in Fig. 4.9. This specific structure of the parasitic pixel layer has been chosen to reduce the mutual coupling between the individual radiators of the MRAA. The three separate structures are then aligned and assembled together, where a 6 mm thick polymethacrylimide foam is used between driven patches and the layer containing parasitic pixel surfaces.

4.2.3 MRAA Working Mechanism and Gain

Background on Linear Antenna Arrays: A typical linear antenna array consists of a

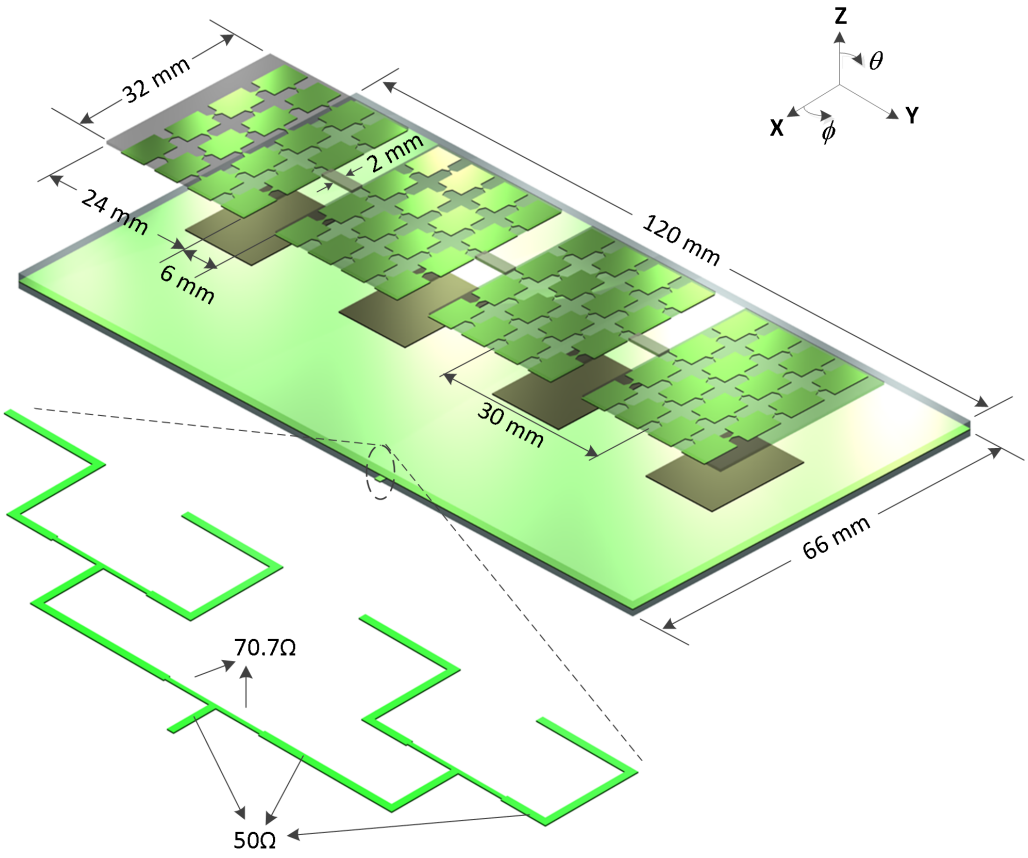

Fig. 4.9: 3-D schematic and feeding network of 4×1 linear MRAA.

number of identical antenna elements, where each element may be individually controlled in phase and amplitude. Let us consider the 4×1 linear array configuration, shown in Fig. 4.10, where the centers of the individual radiators lie on the y-axis with inter-element spacing being d.

As is well known, the normalized far-field radiation pattern of the array, $F(\theta, \phi)$ can be found by using the *principle of pattern multiplication* [8–12], which is given as

$$F(\theta, \phi) = E_a(\theta, \phi) \times F_a(\theta, \phi). \tag{4.1}$$

In Eq. (4.1), $E_a(\theta, \phi)$ is the normalized pattern of the individual radiators, which is also called *element factor*. $F_a(\theta, \phi)$ is the normalized *array factor*, which, for uniform amplitude excitations in the y-z plane ($\phi = \pi/2$), is given as follows:

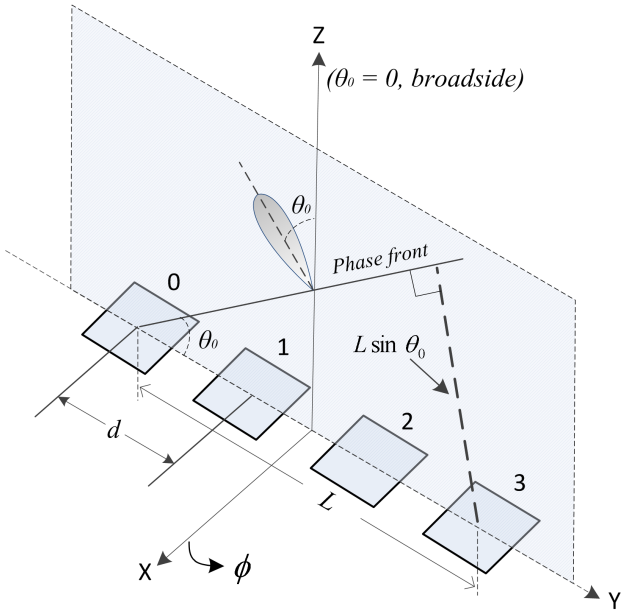

Fig. 4.10: A linear antenna array composed of antenna elements with fixed radiation properties.

$$F_a(\theta) = \frac{\sin[\frac{N\pi d}{\lambda_0} * (\sin\theta - \sin\theta_0)]}{N\sin[\frac{\pi d}{\lambda_0} * (\sin\theta - \sin\theta_0)]}. \tag{4.2}$$

In Eq. (4.2), $N = 4$ is the total number of array elements, and $(\theta = \theta_0)$ is the beam steering direction in y-z plane, for which the array factor is maximum. This array pattern occurs at the center frequency of f_0, when each array element is fed by the complex excitations with uniform amplitude of a_0, and progressive phase shift from element to element, $k_0 d\sin\theta_0$. The complex excitations are given as

$$a_n = a_0 e^{-jk_0 nd\sin\theta_0} \quad (n = 0, 1, 2, 3), \tag{4.3}$$

where $k_0 = 2\pi/\lambda_0$ is the free space wave number at the center frequency of f_0, and n indicates the element number of each individual radiator of the array with first element having *n=0*. From Eq. (4.1)-(4.3), it is evident that the radiation pattern of the array is solely controlled by the array factor. The element factor $E_a(\theta, \phi)$ is fixed by the initial design of the individual radiators, which means that the radiation properties of the individual

radiators cannot be changed, and thus the element factor does not play a role in beam-steering function.

A factor related to an antenna array is the concept of pattern "squint." When the operating frequency changes from f_0 to f_1, the phase front also changes. This, in turn, results in a shift in the original steering angle that goes from θ_0 to θ_1, thereby causing pattern-squint problem. This is also the main limiting factor of the array bandwidth. Another issue associated with a linear array is the *scan loss*. This is due to the broadening beamwidth of the array factor, when it is steered away from the broadside direction. The result is a reduction in the array gain, which becomes significant as the beam is steered further away from the broadside.

As will be investigated in the following section, an MRAA has individual radiators of which radiation properties, such as maximum beam directions and sense of polarizations, can be changed. In other words, the element factor is not fixed and has variable properties. This important additional degree of freedom translates into higher array gain, polarization reconfigurability, and beam-tilt capability not only in *y-z* plane but also in *x-z* plane. Also, the scan loss inherit to standard array is alleviated for the MRAA, when the beam is steered in the *x-z* plane.

The Gain of the MRAA Steering in the x-z Plane: For the MRAA steering in the *x-z* plane, the radiation pattern of the array is not related to the array factor as it does not take effect in the *x-z* plane. The beam steering in this plane is accomplished by the beam-steering capabilities of the individual MRAs of the array. Irrespective of the beam-steering angle, there would be no phase difference from element to element ($\Delta\alpha = k_0 d \sin\theta_0 = 0$), thereby the phase front always stays parallel to the *y*-axis, along which the array elements are arranged as shown in Fig. 4.11. This also indicates that there is no need to employ phase shifters in order to introduce the progressive phase shift between array elements, and thus achieve beam-steering. Therefore, when the modes of operation of the individual MRAs of the MRAA correspond to the beam-steering modes ($\theta_{xz} = 30^o, 0^o, and -30^o$), with either linear and circular polarizations, in the *x-z* plane, the realized gain pattern of

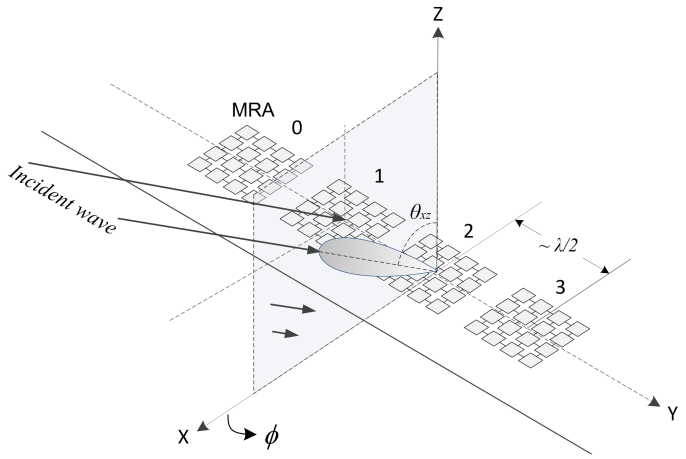

Fig. 4.11: 4×1 linear MRAA for beam-steering in the x-z plane. The individual MRAs are arranged on $y-$axis with the inter element spacing d $\approx$ half-wavelength.

the MRAA, $G_T(\theta)$, in this plane is simply the summation of the realized gain patterns of individual MRAs:

$$G_T(\theta) = \sum_n G_{en}(\theta) \quad (n = 0, 1, 2, 3) \quad (x - z \ plane). \tag{4.4}$$

In Eq. (4.4), $G_{en}(\theta)$ represents the *imbedded* realized gain pattern of the individual n^{th} MRA element in the x-z plane. The term "*imbedded*" is used to emphasize that an individual gain pattern is obtained when the corresponding MRA is excited, while the other MRAs are terminated with matched loads. Therefore, the effects of mutual coupling among array elements are taken into account when calculating $G_{en}(\theta)$for each individual radiator of the array.

It is worth noting that as the array factor does not take effect in the x-z plane, the standard linear array cannot perform beam-steering in this plane. As is well known, for the linear array composed of antenna elements with fixed properties as shown in Fig. 4.10, the beam steering is solely controlled by the array factor of which maximum occurs in the direction of $\theta = \theta_0$, due to the progressive phase shift of $k_0 d \sin\theta_0$ between adjacent array elements. On the other hand, for the MRAA, as the beam-steering is controlled by the variable element factor, the problems such as scan loss and beam-squint associated with the

progressive phase shift between array elements are alleviated in the *x-z* plane.

Under ideal conditions, where the effects of the mutual coupling are ignored, all elements have identical realized-gain patterns, $G_{en}(\theta) = G_e(\theta)$ and from the principle of superposition given in Eq. (4.4), the realized array gain is

$$G_T(\theta) = N \times G_e(\theta) \quad (x - z\ plane). \tag{4.5}$$

From Eq. (4.5), for the 4×1 linear MRAA as shown in Fig. 4.11, $G_T(\theta)$ would be 6 dB higher than $G_e(\theta)$ ($N = 4, d \approx 0.5\lambda$). If the individual MRAs are set to operate in the beam-steering mode of $\theta_{xz} = 30^o$, the simulation and measurement results for $G_e(\theta_{xz} = 30^o)$ indicate ∼9.1 dB, as given in section 4.2.1. This means that $G_T(\theta)$=15.1 dB, which is the maximum array gain. The simulation and measurement results show that the imbedded realized gains of MRA elements for $\theta_{xz} = 30^o$ with n=0,1, 2, 3 are 8.2 dB, 6.9 dB, 6.9 dB, 8.3 dB, respectively. Using Eq. (4.4) yields that $G_T(\theta) = 13.7$ dB. These results prove that the effects of mutual coupling are significant and must be taken into account in evaluating array performance. In particular, the close proximity of the parasitic pixel surfaces of adjacent MRAs, with an edge to edge distance of $\sim 0.12\lambda$ is the main contributing factor to mutual coupling effects.

MRAA Steering in y-z Plane: The working mechanism of the MRAA steering in the *y-z* plane is similar to the working mechanism of a standard linear array described in the *background* section. However, the additional degree of freedom provided by the variable radiation properties of the individual MRA elements combined with the array factor in the *y-z* plane significantly enhances the MRAA performances as compared to those of standard array.

When the MRAA performs the beam-steering in the *y-z* plane, the individual MRA elements are also set to operate in the beam-steering modes in the *y-z* plane with beam steering angles of $\theta_{yz} = -30^o$ and 30^o, as shown in Fig. 4.12.

In this case, the realized gain pattern of the MRAA can be expressed as

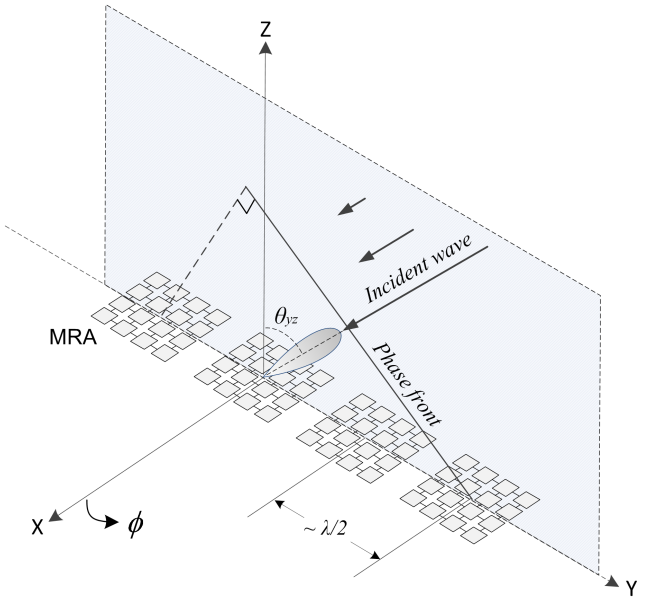

Fig. 4.12: 4×1 linear MRAA for beam-steering in the y-z plane.

$$F_T(\theta) = F_e(\theta, \phi) \times F_a(\theta) \quad (y - z \ plane), \tag{4.6}$$

where $F_a(\theta)$ is the normalized array factor as given in Eq. (4.2) and $F_e(\theta, \phi)$ represents the radiation pattern of an isolated individual MRA. Notice that in Eq. (4.6), the element pattern $F_e(\theta, \phi)$ has variable properties as opposed to the fixed properties of element pattern, $E_a(\theta, \phi)$ given in Eq. (4.1).

For a standard antenna array, which consists of non-reconfigurable patch elements, the side lobe levels increase as the main beam is steered away from broadside. This is due to the fact that the individual element pattern with its maximum in the broadside direction is fixed and cannot be varied. From a practical perspective, this reduces the array gain by a factor which is approximately equal to the reduction of individual element gain for the steered direction, that is, $G_e(\theta_0)/G_e(0)$. To further investigate and show the significant advantage resulting from the individual MRA elements aligning their main beam directions with that of the array factor, Fig. 4.13 compares the simulated beam-steering performances of 4×1 linear MRAA with a standard 4×1 linear array composed of patch antennas with fixed properties.

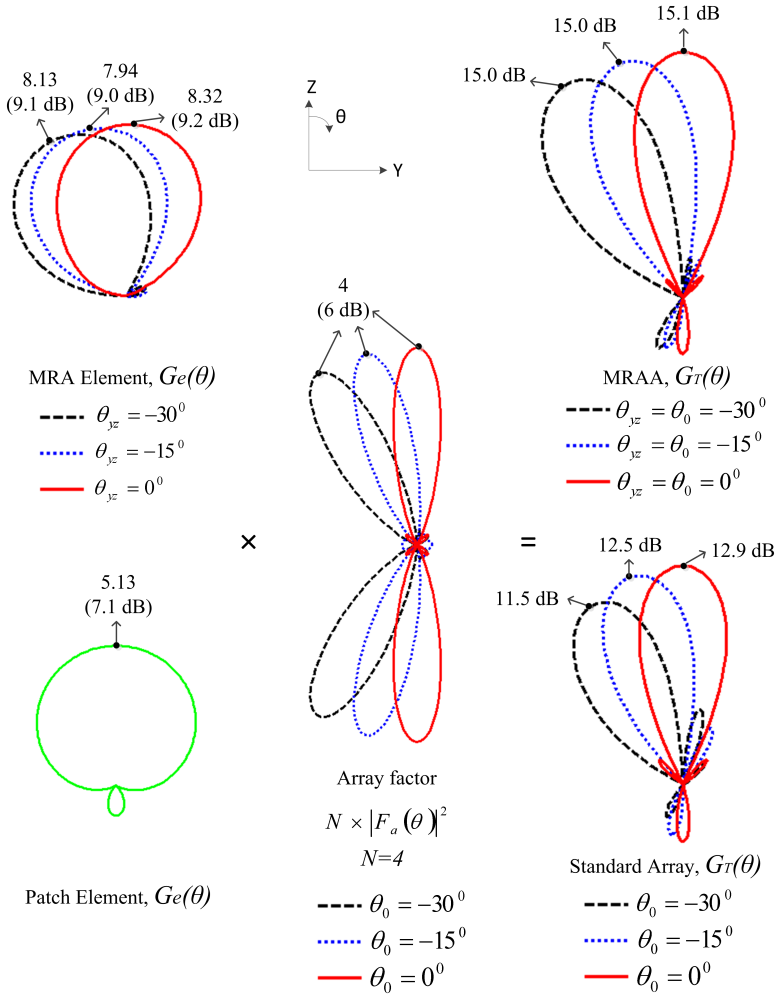

Fig. 4.13: The comparison of the gain patterns of MRAA and of standard linear patch array when the main beam is steered away from the broadside direction into $\theta_0 = -15^o$ and -30^o in the y-z plane ($G_T(\theta) = G_e(\theta) \times N\,|F_a(\theta)|^2$ is used).

Notice that in Fig. 4.13, for the sake of better illustration and explanation, the three beam steering angles of the individual MRA are given as $\theta_{yz} = 0^o, -15^o, -30^o$, although the designs and prototypes investigated in this chapter did not include $\theta_{yz} = \pm 15^o$ due to the reasons for simplicity. As is seen from Fig. 4.13, the realized maximum gain of the MRAA remains almost constant at $\sim$ 15 dB ($\sim$ 6 dB above the maximum gain of the MRA) for all three beam-steering directions. For the standard array, the realized gain reduces from 12.9 dB to 11.5 dB as the main beam is steered off the broadside direction. This is due to the fixed element factor of the standard array of which maximum direction cannot be

aligned with that of the array factor as it is steered off the broadside direction. Also, notice that the side lobe levels are significantly less in the case of MRAA. It should also be noted that in addition to the advantages provided by the variable element factor properties, the MRAA performance also benefits from already improved gain of MRA elements ($\sim$ 9 dB), as compared to the gain of a simple patch antenna ($\sim$ 7 dB), due to the effects of parasitic pixel surface.

Finally, it should be noted that for a given beam direction MRAA can easily achieve polarization reconfigurability as its individual MRA elements can change the sense of polarization between linear and circular polarizations. This work demonstrated the polarization reconfigurability for the beam steering in x-z plane only, but it could also be accomplished for the y-z plane by further optimizing the pixel surface of the parasitic layer. Polarization reconfigurability, of course, is also possible for a standard array but at the cost of increased complexity due to the additional devices such as hybrids and power dividers required.

4.3 MRAA: Measurements vs. Simulations

To validate the theoretical analyses and simulated results of the MRAA, three prototypes have been fabricated. The radiation and impedance characteristics of these prototypes have been measured and compared with those of the simulated results. Each one of these prototypes represents one of the modes of operation, which are the beam steering modes in the x-z plane ($\theta_{xz} = -30^o, 0^o, 30^o$) with linear polarizations. These prototypes were chosen for simplicity as the MRAA performs beam steering in the x-z plane without needing to employ the phase shifters. The design and structure of the MRAA have been presented in section 4.2.2, where the 3-D schematic is depicted in Fig. 4.9. The MRAA prototypes were designed to operate at the center frequency of $\sim$ 5.5 GHz.

Figures 4.14 and 4.15 show the simulated and measured reflection coefficients for the $\theta_{xz} = 0^o, 30^o$, and -30^o modes of operation with linear polarization. Measurement results agree well with the simulations indicating that the common impedance bandwidth for these modes is $\sim 3\%$ around the center design frequency of 5.5 GHz.

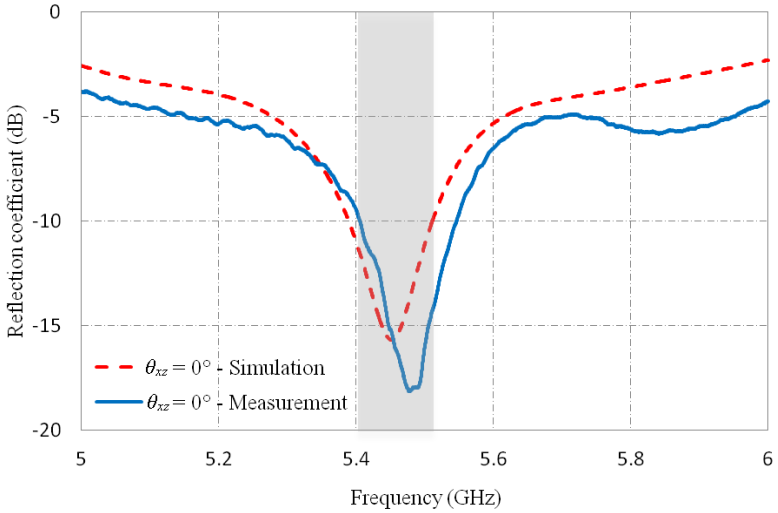

Fig. 4.14: Measured and simulated reflection coefficients of MRAA prototypes for beam steering angle $\theta_{xz} = 0^o$ with linear polarization.

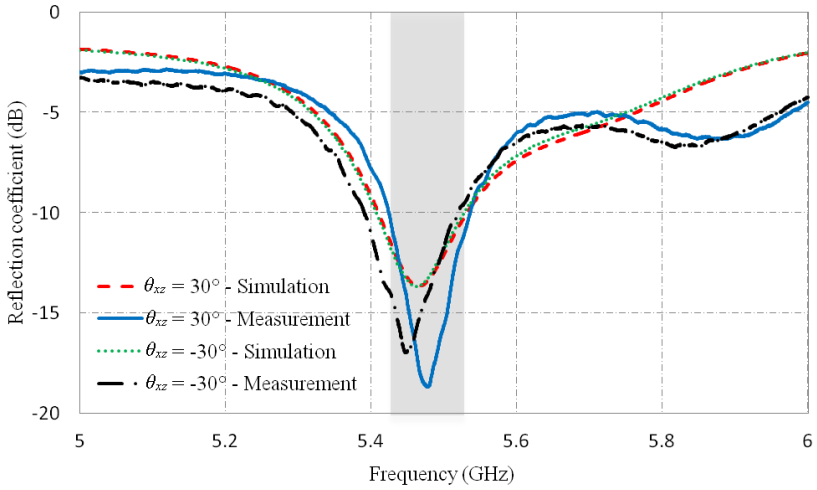

Fig. 4.15: Measured and simulated reflection coefficients of MRAA prototypes for beam steering angles $\theta_{xz} = 30^o$ and $\theta_{xz} = -30^o$ with linear polarization.

It should be noted that one of the main design challenges of a multi-functional reconfigurable antennas is to optimize a desired parameter while maintaining the integrity of other design parameters. In this case, while the beam direction with maximum gain is optimized the impedance bandwidth ($\sim 3\%$) and polarization state (linear polarization) are maintained at required performance limits. This is accomplished by employing an efficient multi-objective genetic algorithm in conjunction with a full-wave design tool.

The measured and simulated radiation patterns in terms of realized gain associated with $\theta_{xz} = 0^o$, and $\theta_{xz} = 30^o$ and -30^o are shown in Figs. 4.16 and 4.17, respectively. These patterns are cut at the center resonant frequency of interest (~5.5 GHz). The simulated and measured results agree well indicating that the realized gain values are 13.5± 0.2 dB for all three beam-steering angles. These results are also in excellent agreement with those of obtained by using Eq. (4.4), $G_T(\theta) = \sum_n G_{en}(\theta) \quad (n = 0, 1, 2, 3)$. For example, the imbedded realized gains of MRA elements for $\theta_{xz} = 30^o$ and -30^o with n=0,1, 2, 3 are 8.2 dB, 6.9 dB, 6.9 dB, and 8.3 dB, respectively, which yields $G_T(\theta) = 13.7$ dB by using Eq. (4.4).

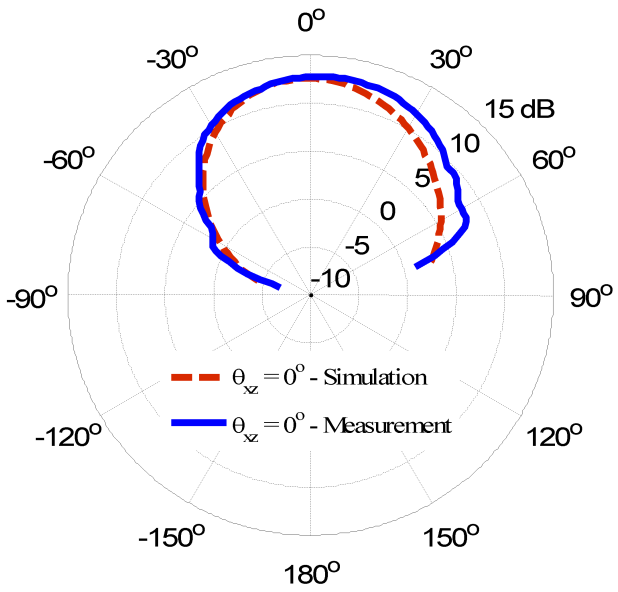

Fig. 4.16: Measured and simulated realized gain patterns of the MRAA prototypes at 5.5 GHz for $\theta_{xz} = 0^o$.

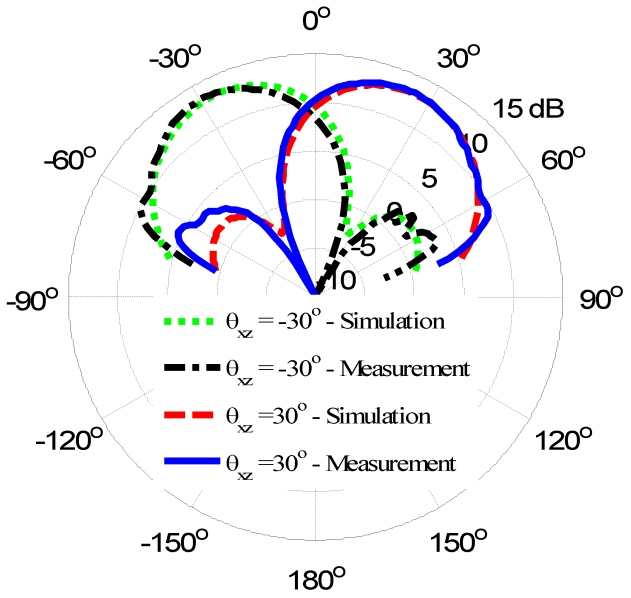

Fig. 4.17: Measured and simulated realized gain patterns of the MRAA prototypes at 5.5 GHz for $\theta_{xz} = 30^o$ and $\theta_{xz} = -30^o$.

4.4 Conclusions

Ever increasing popularity of smartphones, tablets, and cloud computing, to name a few, has been exceedingly fuelling the demand for higher data rates during the last few years. Given that the radio spectrum is a finite natural resource, the next generation wireless systems must employ spectrally efficient technologies. This chapter has presented the initial efforts towards developing a new class of antenna array called multi-functional reconfigurable antenna array (MRAA) with the main goal of enhancing the spectral efficiency of existing and future wireless networks. The MRAA presented in this chapter is formed by the linear combination of four (4×1) identical multi-functional reconfigurable antenna (MRA) elements. The individual radiators (MRAs) of the MRAA possess variable radiation properties; thereby the element factor of the MRAA becomes variable introducing an important additional degree of freedom in enhancing array performances. Compared to a standard linear array with a fixed element pattern, the MRAA has higher array gain, achieves polarization reconfigurability, and beam-tilt capability not only in y-z plane but also in x-z plane, which is perpendicular to the line on which the array elements are arranged.

The beam steering in the x-z plane does not need phase shifters and solely relies on the variable properties, i.e., beam-steering capabilities, of the individual radiators of the array. Therefore, the problems such as scan loss and beam-squint associated with the progressive phase shift between array elements are alleviated. On the other hand, the beam-steering in the y-z plane is accomplished through the combination of array factor and variable element factor. The joint optimization of the array factor with the element factor results in higher array gain, which does not degrade as the beam is steered away from the broadside.

The variable properties, which are the three steerable beam directions ($\theta_{xz} = -30^o$, 0^o, 30^o) with linear and circular polarizations in the x-z plane and another two steerable beam directions ($\theta_{yz} = -30^o, 30^o$) in the y-z plane with linear polarization of the individual MRA, as well as those of the MRAA, are accomplished by reconfiguring the geometry of the parasitic pixel surface. This surface consists of a grid of 4×4 electrically small rectangular-shaped metallic pixels for each individual radiator, where the adjacent pixels can be connected and disconnected by means of switching. For simplicity these connections are taken either as perfect short or perfect open circuits. To validate the theoretical analyses and simulations, various MRA and MRAA prototypes operating in the frequency range of 5.4 - 5.6 GHz have been fabricated and measured. The good agreement between measured and simulated results confirmed the accuracy of the theoretical results. The realized gain values of the MRAA prototypes, which represents the beam steering modes in the x-z plane ($\theta_{xz} = -30^o, 0^o, 30^o$) with linear polarizations, were found to be 13.5$\pm$0.2 dB. These gain values are 2-3 dB higher than those of the standard array composed of patch elements with fixed properties.

It should be noted that although in this chapter the steering angles are chosen to be $\theta = -30^o, 0^o$ and 30^o, steering in other directions such as $\theta = \pm 5^o, \pm 10^o, \pm 15^o, \pm 20^o$, etc., along with polarization reconfigurability both in the x-z and y-z planes would be possible by further optimizing the parasitic pixel surface. As is well known the design and integration of the real switching elements along with the associated bias circuitry within the antenna structure is a critically important engineering task. This task must be accomplished without

presenting any deleterious effect on the antenna performance. From this perspective, one of the advantages of the presented MRAA is the separation of the driven patch layer from the reconfigurable parasitic layer including the switching network, which relaxes the design constraints imposed on these two layers by each other. The results and findings presented in this chapter are providing important insight and guidance to the ongoing prototype developments, which include active switching devices integrated within the parasitic pixel surface structure of the MRAA.

Chapter 5

A Beam-Steering Reconfigurable Antenna for WLAN Applications

5.1 Introduction

Wireless communication technology has grown rapidly in recent years. The IEEE 802.11 b/g standards operating in the 2.4 GHz band have been widely accepted and used in numerous wireless products such as routers, cell phones, and laptops. However, for such systems to achieve the desired high data rate performance, relatively large signal-to-noise ratio (SNR) is required since some other electronic devices such as Bluetooth and microwave oven also operate in the 2.4 GHz band and present noise. In this chapter, the presented MRA is capable of creating nine modes of operation by configuring the surface geometry of the parasitic layer, where 3×3 electrically small square-shaped metallic pixels (parasitic pixel surface) are connected by PIN diode switches with ON/OFF status placed in between the pixels. The modes of operations are nine steerable beam directions ($\theta \in \{-30^o, 0^o, 30^o\}; \phi \in \{0^o, 45^o, 90^o, 135^o\}$) operating in 802.11 b/g band. With the beam steering capability, leakage (interference) both from and to the node of interest can be minimized in unintended directions while the SNR can be maximized in the desired direction. Full-wave analyses by HFSS [37] and multi-objective genetic algorithm optimization [42–44] were jointly employed to determine the interconnecting PIN diode switches status (i.e., ON/OFF) corresponding to the targeted nine modes of operation.

The advantages of the MRA as compared to the antenna presented in Chapter 4 [40] can be summarized as follows: 1) the beam steering capability is enhanced. The presented MRA can perform beam steering in nine directions in the semi-sphere space ($\theta \in \{-30^o, 0^o, 30^o\}; \phi \in \{0^o, 45^o, 90^o, 135^o\}$) instead of only five directions ($\theta \in \{-30^o, 0^o, 30^o\}$;

$\phi \in \{0^o, 90^o\}$). 2) The parasitic surface only consists of 3×3 metallic square pixels instead of 4×4 metallic rectangular pixels, thus the complexity of the MRA is reduced. 3) Real PIN diode switches have been used instead of ideal perfect open/short connection, thus providing insight in the practical limitations of the antenna. The impedance and radiation characteristics of the fabricated individual MRA prototypes were measured. The measured results were compared with those of the simulations, indicating an average of ∼6.5 dB realized gain over the frequency band of 2.4-2.5 GHz for all modes of operations. The beam steering capability and associated system level gains of the MRA was also tested in an experimental system setting based on an IEEE 802.11 b/g system in a typical indoor environment. The results confirm the advantages of the MRA and show that the proposed MRA equipped system achieves ∼6 dB SNR gain compared to the legacy omni-directional antenna equipped system.

5.2 Antenna Structure and Working Mechanism

5.2.1 MRA Design and Component Models

Structure of the MRA: The 3-D schematic and cross section view of the MRA are depicted in Fig. 5.1. This MRA employed aperture-coupled feed mechanism for RF feeding similar to the MRA presented in Chapter 4 [40]. The main two components of the MRA architecture are, namely, the driven patch antenna and parasitic layer. The driven patch ($19.3 \times 19.3\ mm^2$) is designed to operate at in the frequency band of 2.4-2.5 GHz and is fed by a 50-Ohm microstrip line through an aperture ($21.4 \times 1.4\ mm^2$) etched on the center of the common ground plane. The feed layer ($90 \times 90 \times 0.508\ mm^3$) and patch layer ($90 \times 90 \times 3.408\ mm^3$) are built respectively by using the substrate Rogers 4003C ($\varepsilon_r = 3.55, \tan\delta = 0.0021$). The same substrate ($98 \times 90 \times 1.524\ mm^3$) is used to form the parasitic layer above the driven patch. Notice that there is a 7.62 mm gap between the parasitic layer and driven patch antenna, where the gap is filled with the RO4003C. The reconfigurable parasitic surface, which consists of 3×3 square-shaped metallic pixels connected by PIN diode switches with ON/OFF status, is formed on the top surface of the

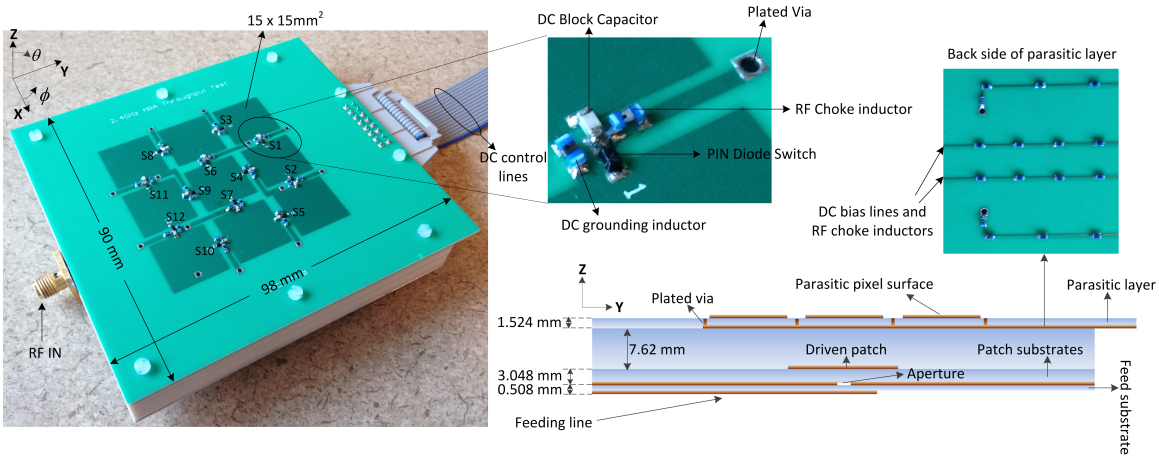

Fig. 5.1: 3-D schematic and the cross section view of the MRA.

parasitic layer with individual pixel size being ($15 \times 15\ mm^2$). Thus the geometry of the parasitic surface can be configured by switching ON/OFF the PIN diode switches. DC bias lines are also formed on the parasitic layer but on the backside of the substrate. Vias are plated through the parasitic layer so that DC bias lines can be connected to the PIN diode switches on the parasitic surface.

Four different kinds of lumped components are used on the parasitic layer as shown in Fig. 5.1. 1) PIN diode switches are used in between all square-shaped pixels. Metallic pixels are connected/disconnected by switching ON/OFF the PIN diode switches to change the geometry of the parasitic surface, which in turn change the current distribution, and thus antenna characteristics. 2) Inductors are placed along the DC bias lines as RF chokes. The SRF (self resonant frequency) of the RF choke is chosen to be around 2.5 GHz, thus RF chokes would appear as high impedance in 802.11 b/g band to minimize the current on the bias lines, thereby minimizing the mutual coupling effects of the bias lines on the antenna performance. 3) Inductors are also placed in between all pixels. In this manner, all the pixels can be DC grounded together to provide ground for DC biasing purpose. The SRF of these inductors was chosen to be the same value as RF chokes to keep the high RF impedance between pixels. 4) DC block capacitors are used to properly bias the PIN diode switches as shown in Fig. 5.1. The SRF of DC block capacitor is around 2.5 GHz to provide low RF impedance in 802.11 b/g band. In this way, the effect of DC block capacitor on RF

performance is minimized.

The manufacturer details [45–47] of the above four components are shown in Table 5.1. The equivalent circuit of the biasing scheme is explained in the following paragraph.

Equivalent Circuit Models used in MRA: The DC biasing scheme of the PIN switch is shown in Fig. 5.2. It can be seen that the four different lumped components mentioned above are required to properly bias the PIN diode. Typically, 1 V DC power supply on the PIN diode would be sufficient to turn on the switch, while 0 V will keep the switch in OFF status.

The equivalent circuit models of these lumped components are obtained by using their scattering parameters provided by the manufacturers and are shown in Fig. 5.3. These equivalent circuit models are used in the design of the MRAs by full-wave HFSS analyses.

5.2.2 Working Mechanism

The working mechanism of an antenna system, which is composed of one driven antenna

Table 5.1: Lumped components used in MRA for WLAN applications.

Manufacturer	Type	Value	SRF
Skyworks SMP1345	PIN diode switch	N/A	N/A
Coilcraft 0603 HP	RF choke	39 nH	2.5 GHz
Coilcraft 0603 HP	DC grounding inductor	39 nH	2.5 GHz
Murata 0603	DC block capacitor	8 pF	2.5 GHz

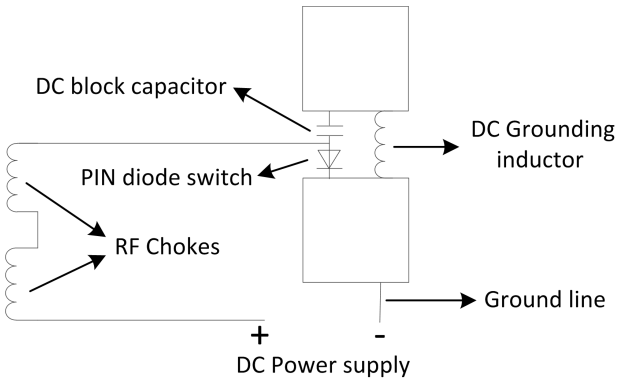

Fig. 5.2: DC biasing scheme of the PIN diode switch.

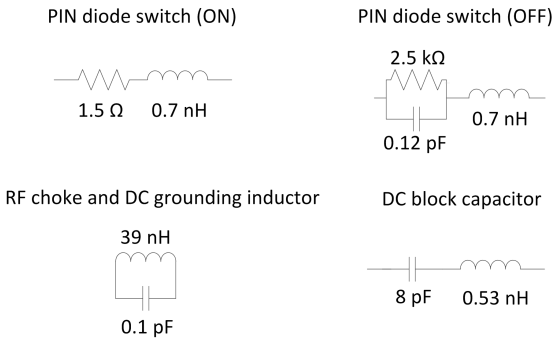

Fig. 5.3: Equivalent circuit models of lumped components.

and multiple parasitic elements, might be described by the theory of reactively controlled directive arrays developed by Harrington [28]. It was shown that the main beam direction of the driven antenna can be directed into a desired direction by the proper reactive loading of the parasitic elements. In the presented MRA, the proper reactive loading corresponds to a specific geometry of the parasitic pixel surface, which is obtained by switching ON/OFF the PIN diode switches between adjacent pixels of this surface.

The presented MRA is aimed to steer its main beam in nine directions in the semi-sphere space ($\theta \in \{-30^o, 0^o, 30^o\}$; $\phi \in \{0^o, 45^o, 90^o, 135^o\}$). Figure 5.4 illustrates the planes in which the beam is steered, and the definitions of the beam-steering angles (θ and ϕ).

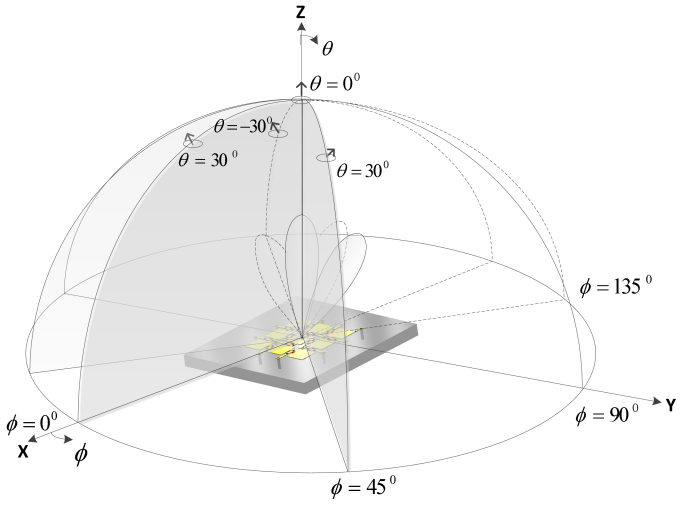

Fig. 5.4: Beam-steering capabilities of an MRA.

5.2.3 Optimization Methodology

To find the optimum switch status for each of the nine beam steering directions, multi-objective genetic algorithm (GA) is utilized [30]. The multi-objective GA is different from the single-objective GA in the sense that it has more than one aim which may conict with each other and should be evaluated simultaneously. There are three objectives/aims need to be satisfied, namely: 1) one of the beam directions of ($\theta \in \{-30^o, 0^o, 30^o\}; \phi \in \{0^o, 45^o, 90^o, 135^o\}$) with maximum gain above 6 dB, 2) desired frequency bandwidth (BW) of $\sim 4\%$ covering 2.4-2.5 GHz, and 3) linear polarization with axial ratio above 10 dB in the maximum gain direction. Thus the objective functions are defined as below:

$$\begin{aligned} obj_1 &= Gain(f_o, \theta, \phi) && (Gain \geq 6dB), \\ obj_2 &= BW(|S11|, -10dB) && (BW \geq 4\%), \\ obj_3 &= AR(f_o, \theta, \phi) && (AR \geq 10dB), \end{aligned} \tag{5.1}$$

where f_0 is the center frequency of the 802.11 b/g band as 2.45 GHz, θ and ϕ describe the desired beam steering direction. $|S11|$ represents the magnitude of reflection coefficient, and AR is the axial ratio for polarization. These three criteria are applied simultaneously in multi-objective genetic algorithm, and in conjunction with full-wave EM analysis to find the optimized switch configurations resulting in each of the nine beam steering directions. Note that corresponding to beam directions of ($\theta \in \{-30^o, 0^o, 30^o\}; \phi \in \{0^o, 45^o, 90^o, 135^o\}$), nine optimization problems are defined. The further details of the multi-objective algorithm [30] are omitted here.

5.3 Antenna Measurements vs. Simulation

To validate the theoretical analysis and simulated results of the MRA, prototypes were fabricated and measured. The switch configurations for all nine desired modes are shown in Table 5.2, where S1- S12 represent the 12 PIN diode switches used in the design as shown in Fig. 5.1 (0 represents that the PIN diode switch is OFF, 1 represents that the

PIN diode switch is ON). The MRA prototype was designed to operate in the 802.11 b/g frequency band (2.4-2.5 GHz). The reflection coefficients and radiation patterns in terms of realized gain have been measured for all the modes. Figure 5.5 show the simulated and measured reflection coefficients for the modes on $\phi = 0^o$ plane with $\theta = -30^o, 0^o, 30^o$. It can be seen that the common bandwidth covers IEEE 802.11 b/g frequency band. Figure 5.6 shows good agreement between simulated and measured realized gain patterns for these three modes indicating that the maximum realized gain of the MRA is ∼6.5 dB in each mode. Note that only co-polarization components are plotted in the patterns since cross-polarization components are less than -10 dB and thus are not shown. Simulated and measured reflection coefficients and realized gain patterns for other modes on the planes ($\phi \in \{45^o, 90^o, 135^o\}$) are shown in Figs. 5.7, 5.8, and 5.9, respectively. It can be seen that there is also good agreement between simulation and measurement for these modes.

Table 5.2: Switch configurations for nine modes of operation.

θ	ϕ	S1	S2	S3	S4	S5	S6	S7	S8	S9	S10	S11	S12
0^o	0^o	0	0	0	0	0	0	0	0	0	0	0	0
30^o	0^o	0	1	1	0	0	1	0	1	0	0	0	1
-30^o	0^o	1	0	0	0	1	0	1	0	0	1	1	0
30^o	45^o	1	0	1	0	0	1	0	1	0	0	0	1
-30^o	45^o	1	0	0	0	1	1	0	0	0	0	1	0
30^o	90^o	1	0	0	1	0	0	1	0	0	0	1	1
-30^o	90^o	0	1	1	0	0	0	1	1	1	0	1	1
30^o	135^o	0	1	0	0	1	0	1	0	0	1	1	0
-30^o	135^o	0	1	1	0	0	1	0	1	0	0	1	0

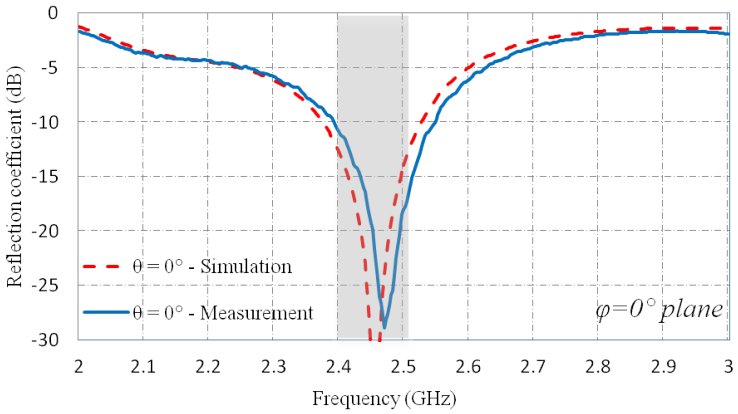

(a)

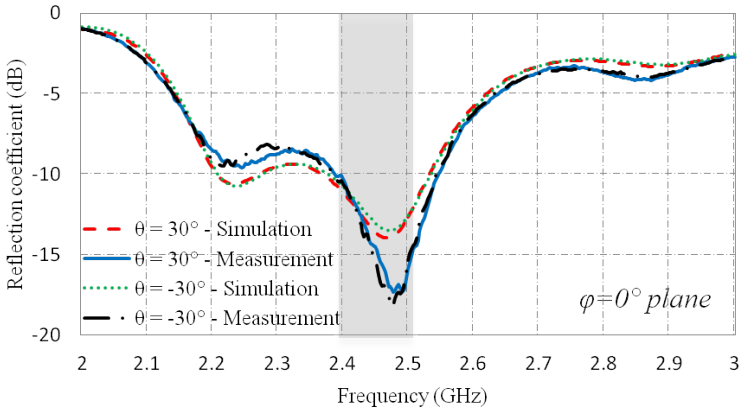

(b)

Fig. 5.5: Measured and simulated reflection coefficients of the MRA prototype for beam steering angles (a) $\theta = 0^o$ on $\phi = 0^o$ plane, (b) $\theta = 30^o$ and $\theta = -30^o$ on $\phi = 0^o$ plane.

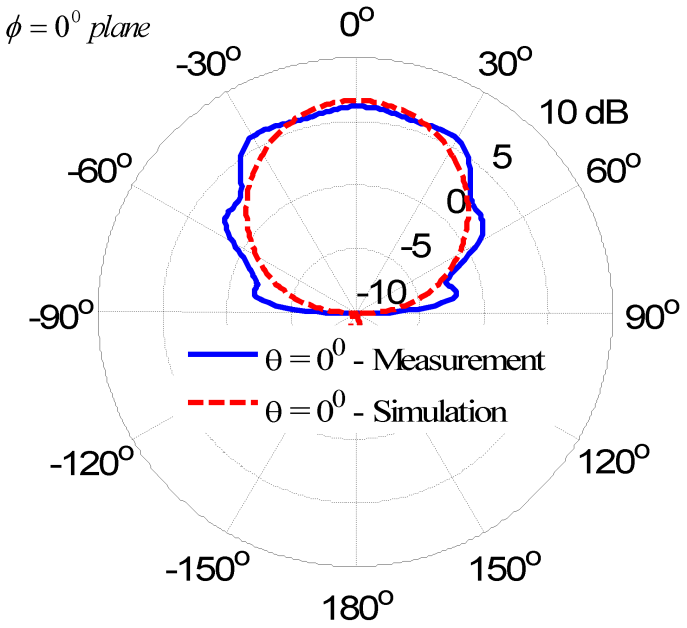

(a)

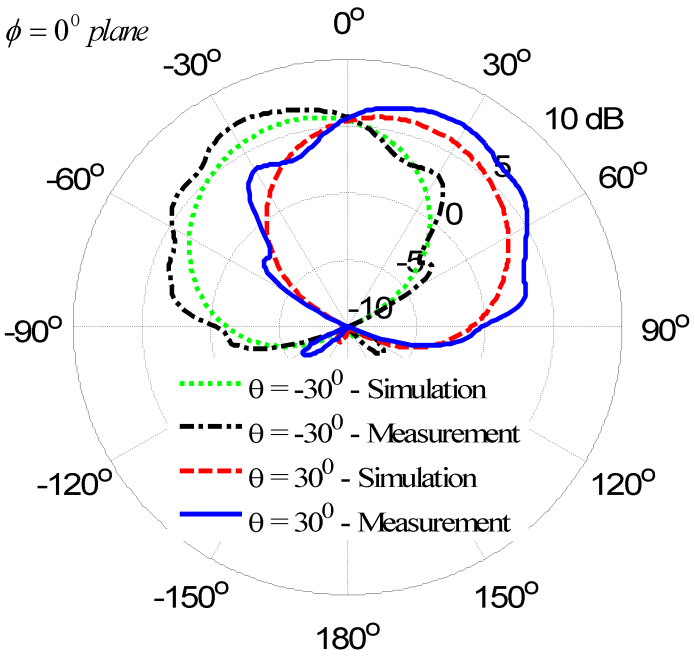

(b)

Fig. 5.6: Simulated and measured realized gain patterns of the MRA prototype for (a) $\theta = 0^o$ on $\phi = 0^o$ plane, (b) $\theta = 30^o$ and $\theta = -30^o$ on $\phi = 0^o$ plane at 2.45 GHz.

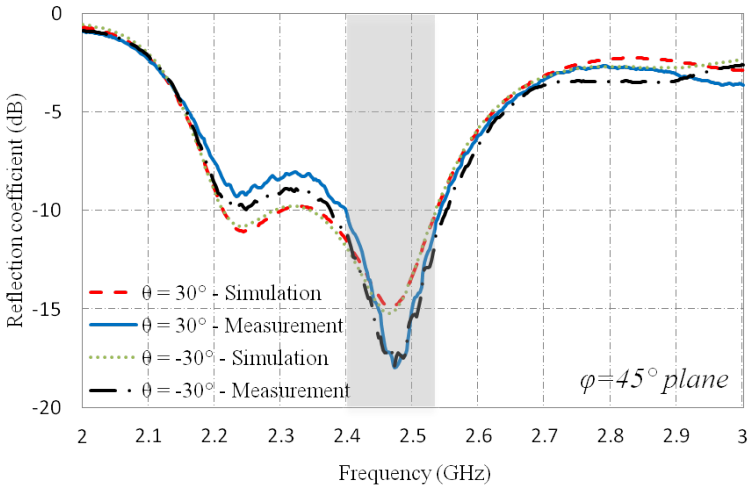

(a)

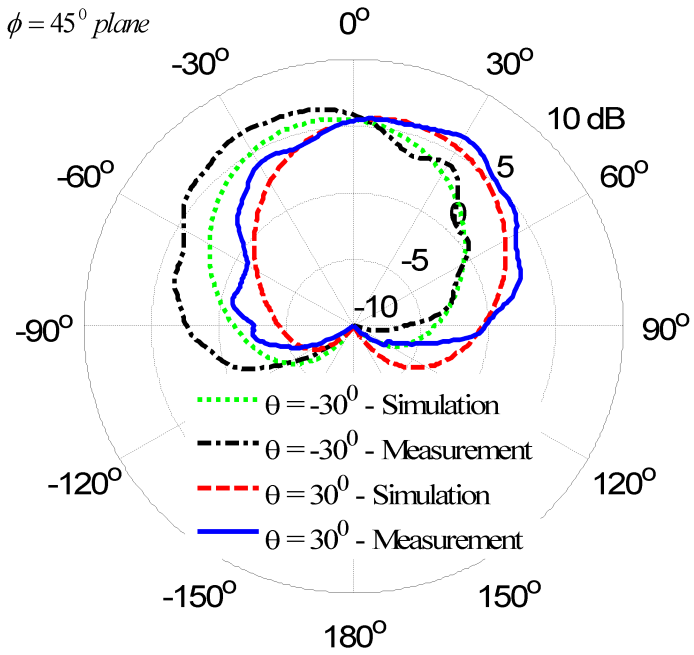

(b)

Fig. 5.7: Simulated and measured (a) reflection coefficients, (b) realized gain patterns of the MRA prototype for $\theta = 30^o$ and $\theta = -30^o$ on $\phi = 45^o$ plane at 2.45 GHz.

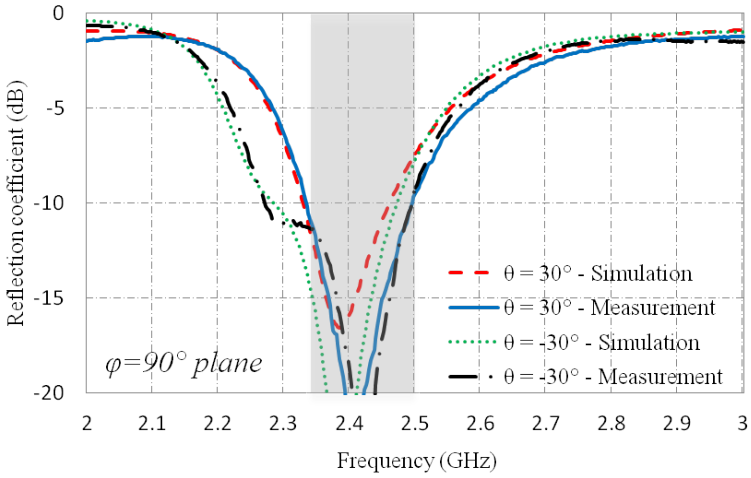

(a)

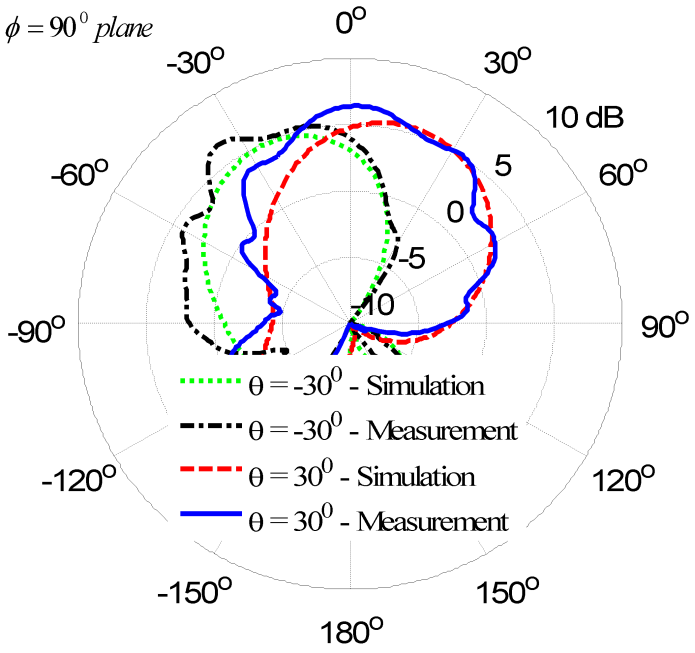

(b)

Fig. 5.8: Simulated and measured (a) reflection coefficients, (b) realized gain patterns of the MRA prototype for $\theta = 30^o$ and $\theta = -30^o$ on $\phi = 90^o$ plane at 2.45 GHz.

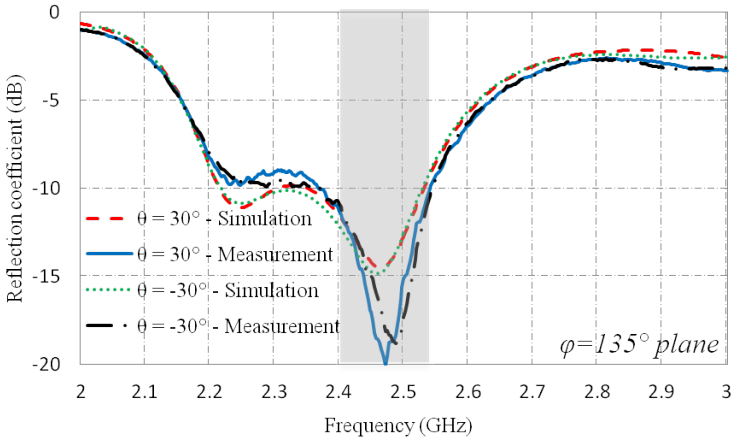

(a)

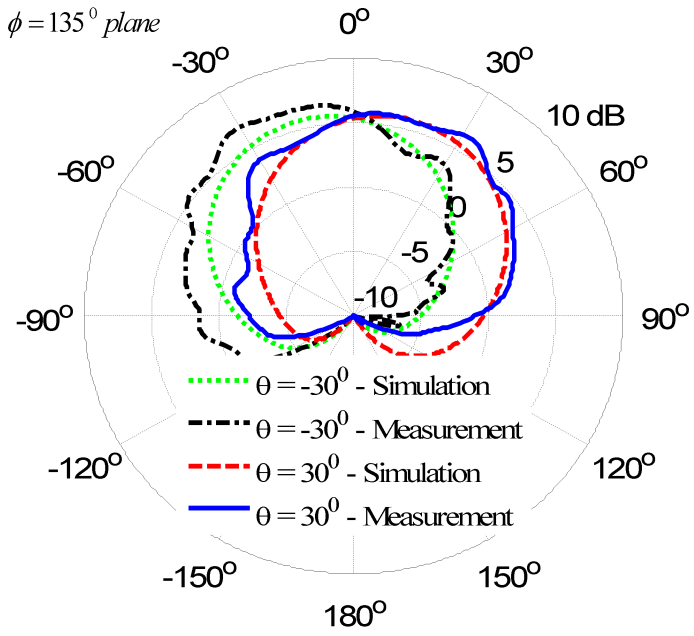

(b)

Fig. 5.9: Simulated and measured (a) reflection coefficients, (b) realized gain patterns of the MRA prototype for $\theta = 30^o$ and $\theta = -30^o$ on $\phi = 135^o$ plane at 2.45 GHz.

5.4 System Level Tests and Characterizations

In this section, to confirm the advantages of the MRA, the system-level experimental analysis and performance characterization of MRA-based WLAN systems is presented.

5.4.1 Experimental Setup

An MRA-based WLAN system is constructed using the Universal Software Radio Peripheral (USRP) software defined radio (SDR) platform [48]. Each USRP contains a Radio Frequency (RF) transceiver and a Field Programmable Gate Array (FPGA). All USRPs are connected to a host PC through a Gigabit Ethernet connection. The baseband signal processing is performed over the host PC. The baseband signals are streamed to/from the USRPs at a rate of 25M sample/sec. The RF transceivers are then used for real time signal transmission and reception. All experiments are performed in the IEEE 802.11 b/g band at 2.5 GHz carrier frequency with a 10 MHz signal bandwidth.

As shown in Fig. 5.10, the system consists of two nodes communicating to each other. Each node is equipped with one antenna. In this work, one of the two nodes is equipped with an omni-directional antenna, while the other node is equipped with a MRA. The MRA antenna has a total of nine different radiation patterns. The pattern selection is performed through a 12-line digital control cable driven from an FPGA on a Zedboard [49]. The timing of all USRPs and the FPGA that drives the antenna switches are aligned with one reference Pulse Per Second (PPS) signal. Another system architecture where both nodes are equipped with omni-directional antennas is used for comparison purposes.

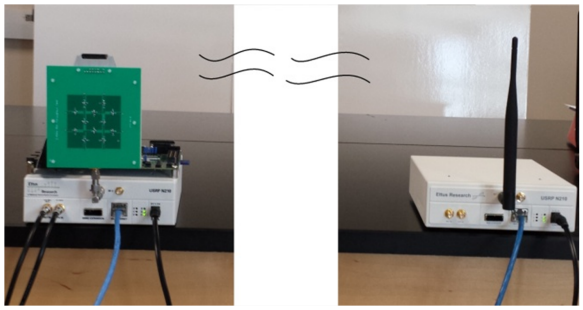

Fig. 5.10: MRA-based wireless system using USRP platforms.

5.4.2 Experimental Framework

Figure 5.11 shows the transmission frame structure used for performance characterization. The transmission frame consists of two main intervals: 1) training interval, and 2) data transmission interval. The training interval consists of nine training segments used for MRA pattern training. The MRA radiation pattern is changed at the segment edge such that, each training segment corresponds to one of the MRA radiation patterns. At the end of the training interval, the received signal power for each pattern is calculated, and the pattern that maximizes the received signal power is selected. During the data transmission interval, useful data transmission takes place. The data transmission interval consists of several data frames that have the same frame structure as in the IEEE 802.11g systems [50]. Each data frame consists of 125 Orthogonal Frequency Division Multi-plexing (OFDM) symbols with 64 subcarriers per OFDM symbol.

5.4.3 Experimental Environment

The experimental analysis is conducted in the Wireless Systems and Circuits Laboratory (WSCL) within Engineering Hall at the University of California, Irvine. Figure 5.12 shows a floor plan for the area where the experiments are performed, and present a typical laboratory environment with measurement workstations, tables, metallic surfaces, etc. The outer walls of the building are either concrete walls or glass walls with steel pillars, while the inner walls are dry walls with steel pillars. To enrich the experimental analysis, the two communicating nodes are placed at different positions inside and outside the laboratory to create a variety of Line Of Sight (LOS) and non-LOS environments. In addition, different MRA orientations are tested such that the two communicating nodes are facing each other, opposite to each other, or side to side.

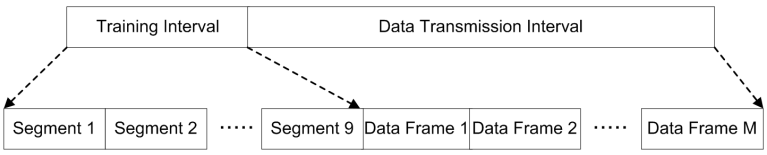

Fig. 5.11: Transmission frame structure.

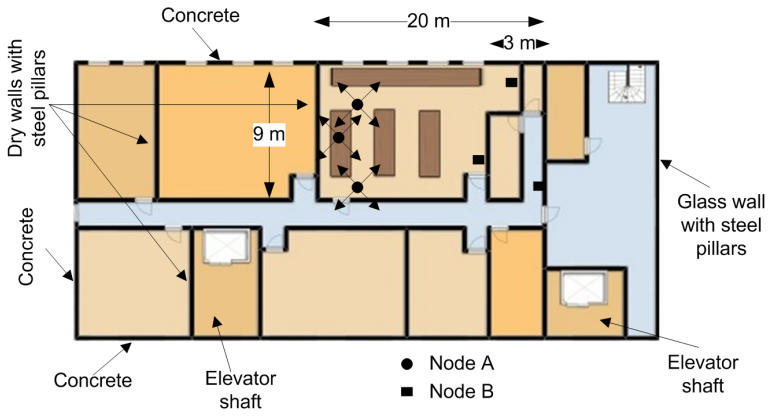

Fig. 5.12: Floor plan for the area where the experiments are conducted.

5.4.4 Experimental Results

In this analysis, the performance of the MRA-based IEEE 802.11g systems is evaluated and compared to the legacy omni-directional antenna based systems. For comparison purposes, three different performance metrics are used: 1) The effective SNR, 2) the achievable rate, and 3) the average un-coded Bit Error Rate (BER). The SNR is defined as the ratio between the received signal power and the total system noise power. One way to calculate the effective SNR in experimental analysis is by calculating the Error Vector Magnitude (EVM) defined as the distance between the received symbols after equalization and the original transmitted symbols. Using the EVM to SNR conversion method [51], the SNR is calculated as $SNR = 1/\overline{EVM}^2$, where $\overline{EVM}$ is the average EVM. The achievable rate is defined as the maximum data rate that the wireless system could achieve at certain SNR. The average achievable rate is calculated in terms of the SNR as

$$R = \frac{1}{N * M} \sum_{m=1}^{N} \sum_{n=1}^{M} log_2(1 + SNR_{m,n}), \tag{5.2}$$

where M, N are the total number of data frames and OFDM symbols per frame, respectively.

Figure 5.13 shows the effective SNR for MRA-based and omni-directional antenna-based systems at different transmit power values. The results show that, using MRA achieves an average of 5-6 dB SNR gain compared to the legacy omni-directional antenna systems.

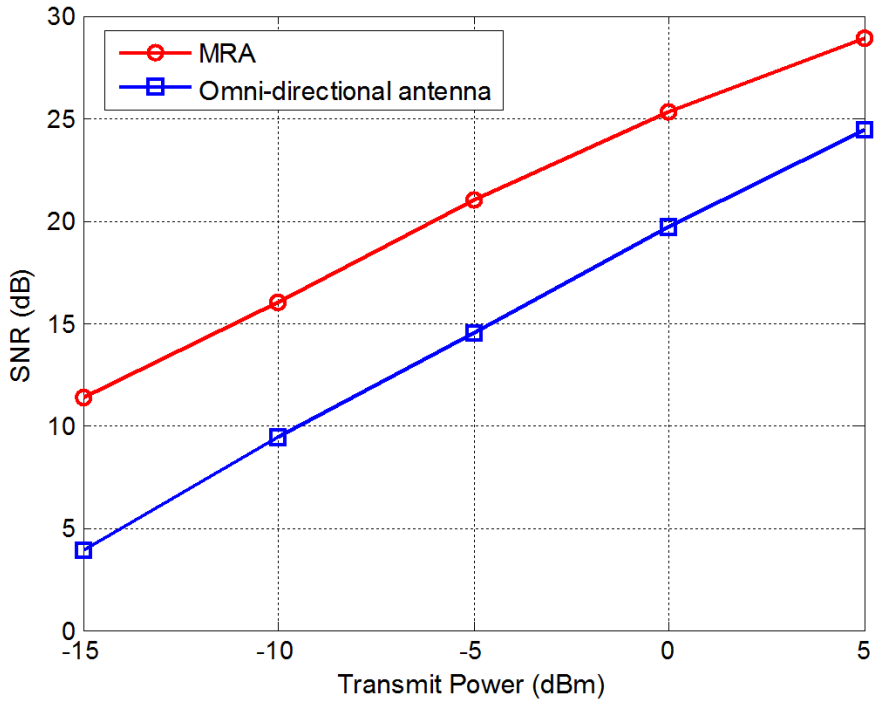

Fig. 5.13: Effective SNR for MRA-based and omni-directional antenna based systems at different transmit power values.

Unlike omni-directional antenna systems, MRA-based systems require pattern training, which negatively impacts the overall system capacity. Therefore, for fair comparison, the MRA training overhead should be considered. In this analysis, the achievable rate of both MRA-based and omni-directional antenna based systems is evaluated. The MRA training overhead is set to ∼0.5% (i.e. MRA training interval/data transmission interval = 0.005). Figure 5.14 shows the achievable rate at different transmit power values when MRA training overhead is considered. The results show that, even after training overhead is considered, MRA-based systems could achieve ∼2 bits/sec/hz more data rate compared to legacy omni-directional antenna systems.

The overall performance is also characterized for different modulation schemes. Figure 5.15 shows the average BER for both MRA-based and omni-directional antenna-based systems. The results show that using MRA achieves ∼5-6 dB SNR gain compared to omni-directional antenna-based systems, which confirms the results shown in Fig. 5.13.

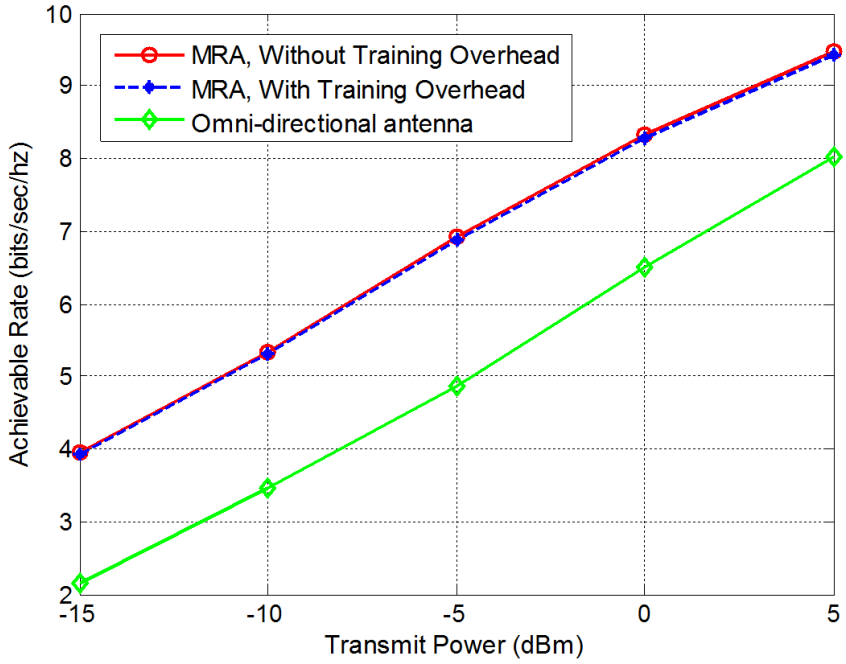

Fig. 5.14: Achievable rate for MRA-based and omni-directional antenna based systems at different transmit power values.

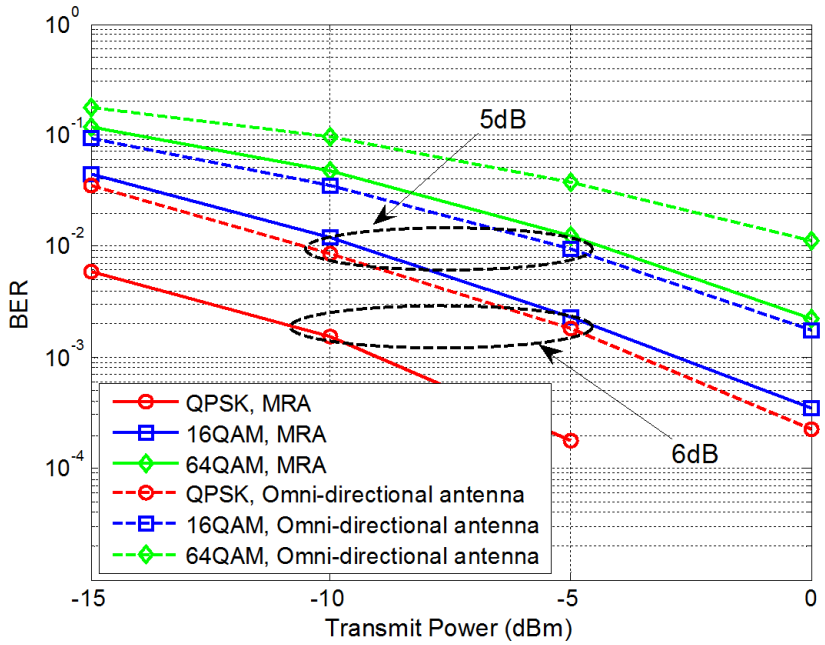

Fig. 5.15: BER for MRA-based and omni-directional antenna based systems at different transmit power values with different modulation schemes.

5.5 Conclusions

This chapter presented a full model of a multi-functional reconfigurable antenna (MRA) with the main goal of enhancing the spectral efficiency of 802.11 b/g networks. The presented MRA is capable of steering its main beam in nine directions ($\theta \in \{-30^o, 0^o, 30^o\}\,; \phi \in \{0^o, 45^o, 90^o, 135^o\}$) by reconfiguring the geometry of the parasitic pixel surface. This surface consists of a grid of 3×3 electrically small square-shaped metallic pixels, and the geometry of this surface is altered by switching ON/OFF the interconnecting PIN diode switches placed between adjacent metallic pixels. To validate the theoretical analyses and simulations, a prototype of MRA operating in the IEEE 802.11 b/g frequency band has been fabricated and measured. The good agreement between measured and simulated results confirmed the accuracy of the theoretical results. The average realized gain values of the MRA prototype are ∼6.5 dB in all modes of operation over the 2.4-2.5 GHz frequency band. The MRA was also implemented in a practical system setting, where the system level experimental performance of an MRA equipped WLAN platform was tested and characterized in typical indoor environments. The results showed that the MRA equipped WLAN systems could achieve an average of 6 dB Signal to Noise Ratio (SNR) gain compared to legacy omni-directional antenna equipped systems with minimal training overhead.

Chapter 6

A Broadband Beam-Steering Reconfigurable Antenna

6.1 Introduction

Wireless communication technology has been growing rapidly in recent years. With new wireless computing network standard released, new products such as routers, laptops and handsets are developed quickly in the market. The recently released 802.11 ac standard which is under Wi-Fi category requires a frequency band from 5.17 GHz to 5.835 GHz (US) which is ∼12% bandwidth. To develop products under this standard using standard microstrip antenna is difficult since a single legacy patch antenna typically only has a bandwidth of ∼3%. Thus, broadband technique is required to cover the whole frequency band for proper operation if a compact design using microstrip antenna is required.

There has been a significant amount of research on broadband techniques to increase the bandwidth of microstrip antenna in the literature [52–56]. In this work, a stacked patch antenna is employed as part of the design to realize the broadband characteristic. The presented MRA consists of an aperture-coupled fed stacked patch antenna with a parasitic layer placed above it (see Fig. 6.1), where the stacked patch antenna is used as the driven element. The MRA is capable of producing three modes of operation by configuring the surface geometry of the parasitic layer, where the 3×2 electrically small rectangular-shaped metallic pixels (parasitic pixel surface) are connected/disconnected by switching ON/OFF PIN diode switches placed in between the specific pixels. The modes of operation are three steerable beam directions ($\theta \in \{-30^o, 0^o, 30^o\}\,; \phi = 0^o$) operating in 802.11 ac band. Full-wave analysis by HFSS [37] and multi-objective genetic algorithm optimization [42–44] are jointly employed to determine the interconnecting PIN diode switches status (i.e., ON/OFF) corresponding to the three modes of operation.

The advantages of the presented MRA as compared to the ones presented before [40,57]

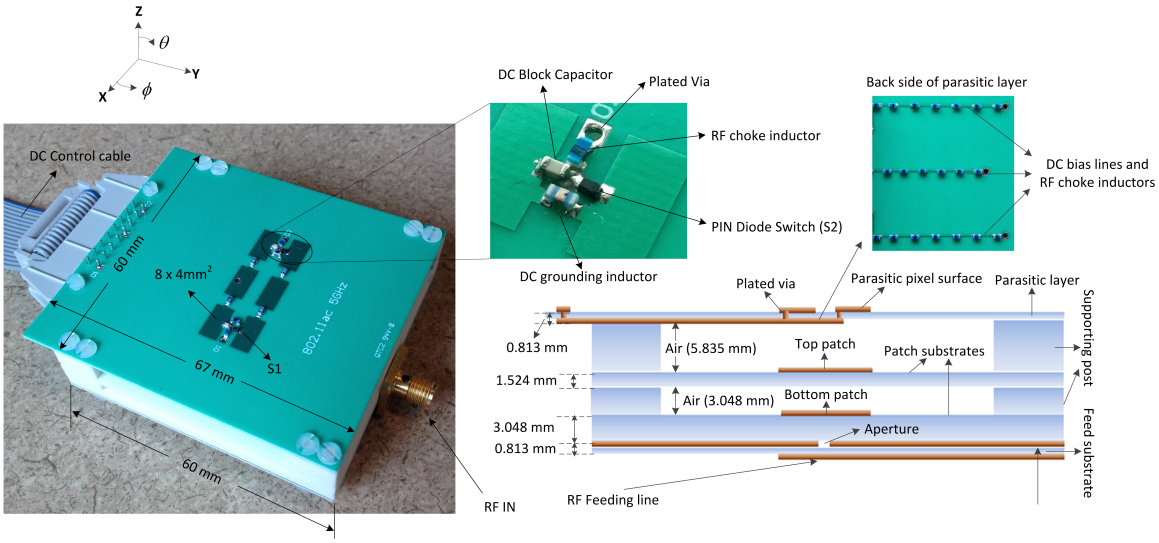

Fig. 6.1: 3-D schematic and the cross section view of the MRA.

can be summarized as follows: 1) The parasitic surface of the MRA consists of 3×2 metallic rectangular pixels, and only two switches are utilized between pixels to achieve beam steering in three directions in the semi-sphere space ($\theta \in \{-30^o, 0^o, 30^o\}\,; \phi = 0^o$). The complexity of the MRA in terms of the number of switches and pixels has been significantly reduced. The major benefit of a much simpler geometry is that the redundancy of the antenna is reduced while the design goal can still be met. 2) Stacked patch with broadband characteristic is used as the driven element of the MRA, thus the bandwidth of the MRA is increased from ~3% to ~15%. 3) The beam steering direction is maintained over the 802.11 ac frequency band in all modes of operations. This integrity of beam steering direction vs. frequency makes this MRA suitable for wireless products where the stability of the antenna performance is the main concern. 4) Air gaps are used among driven stacked patches and parasitic layer. Air gaps enhance the bandwidth of the MRA, significantly reduce the weight of the antenna, and minimize the resistive loss of the antenna.

The advantages of the MRAA architecture include no phase shifter needed for beam steering in certain planes; scan loss can be elevated, etc., where the details can found in Chapter 4.

These advantages of the presented MRA and MRAA can be used to enhance the

capabilities of the IEEE 802.11 ac systems, which will provide significant performance improvement over a MIMO system employing single-function antennas.

6.2 MRA Design and Working Mechanism

The 3-D schematic and cross section view of the broadband MRA are depicted in Fig. 6.1. This MRA employed aperture-coupled microstrip feed mechanism for RF feeding. The main two components of the MRA architecture are, namely, the driven stacked patch antenna and parasitic layer. The driven stacked patch (Top patch: $11.5 \times 11.5\ mm^2$; Bottom patch: $11.3 \times 11.3\ mm^2$) is designed to operate in the 802.11 ac frequency band and fed by a 50-Ohm microstrip line through an aperture ($11.3 \times 0.5\ mm^2$) etched on the center of the ground plane. The feed substrate ($60 \times 60 \times 0.813\ mm^3$) and both patch substrates ($60 \times 60 \times 3.408\ mm^3$, $60 \times 60 \times 1.524\ mm^3$) are built, respectively, by using the substrate, Rogers RO4003C ($\varepsilon_r = 3.55, \tan\delta = 0.0021$). The same substrate ($60 \times 67 \times 0.813\ mm^3$) is used as the parasitic layer above the driven stacked patch. The reconfigurable parasitic surface, which consists of 3×2 rectangular-shaped metallic pixels with individual pixel size being ($8 \times 4\ mm^2$), is formed on top surface of the parasitic layer to provide beam steering capability. DC bias lines are also formed on the parasitic layer but on the backside of the substrate. Vias are plated through the parasitic layer such that DC bias lines can be connected to the PIN diodes on the parasitic surface. Four different kinds of lumped components are used on the parasitic layer as shown in Fig. 6.1. 1) Two PIN diode switches are used in between specific rectangular pixels. Metallic pixels are connected/disconnected by switching ON/OFF the PIN diode switches to change the geometry of the parasitic surface, which in turn change the current distribution, and thus RF characteristic. 2) Inductors are placed along the DC bias lines as RF chokes. The SRF (self resonant frequency) of the RF choke is chosen to be around 5.5 GHz, thus RF chokes would appear as high impedance in 802.11 ac band to minimize the current on the bias lines, thus minimize the effect of the bias lines on the antenna performance. 3) Inductors are also placed in between all the rectangular pixels to connect all the pixels together. In this manner, all the pixels can be DC grounded together to provide Ground for DC

biasing purpose. The SRF of these inductors is tuned for better performance of MRA (i.e., higher gain) for a specific configuration, which basically changes the reactive loading of the parasitic surface. The SRF was finally chosen to be 2.5 GHz. 4) DC block capacitors are used to properly bias the PIN diode switches as shown in Fig. 6.1. The SRF of DC block capacitor is around 5.5 GHz to provide low impedance in 802.11 ac band. In this way, the effect of DC block capacitor on RF performance is minimized.

The product details [45–47] of the above four components are shown in Table 6.1.

The equivalent circuit models of these lumped components are obtained by using their scattering parameters provided by the manufacturers and are shown in Fig. 6.2. These equivalent circuit models are used in the design of the MRAs by full-wave HFSS analyses. The DC biasing scheme of the PIN switch and working mechanism of the MRA is the same as that described in Chapter 4.

Table 6.1: Lumped components used in Broadband MRA.

Manufacturer	Type	Value	SRF
Skyworks SMP1345	PIN diode switch	N/A	N/A
Coilcraft 0603 HP	RF choke	15 nH	5.5 GHz
Coilcraft 0603 HP	DC grounding inductor	39 nH	2.5 GHz
Murata 0603	DC block capacitor	1.6 pF	5.5 GHz

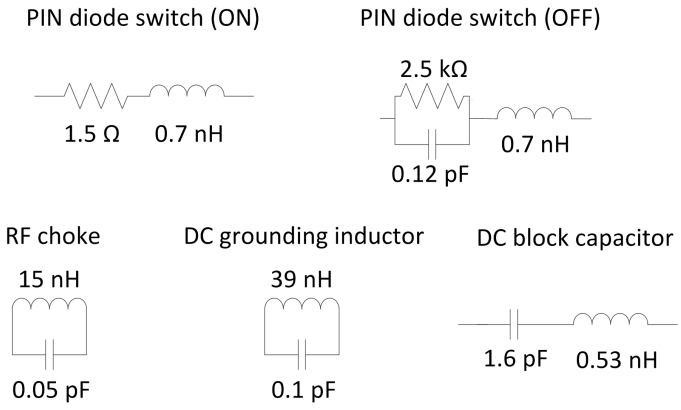

Fig. 6.2: Equivalent circuit models of lumped components.

6.3 Optimization Methodology

The presented MRA and MRAA are aimed to steer its main beam in three directions in semi-sphere space corresponding to three modes of operation ($\theta \in \{-30^o, 0^o, 30^o\}\,; \phi = 0^o$), which is illustrated in Fig. 6.3.

To find the optimum switch status for each of these three beam steering directions, multi-objective genetic algorithm (GA) is employed. There are three objectives/aims need to be satisfied, namely: 1) one of the beam directions of ($\theta \in \{-30^o, 0^o, 30^o\}\,; \phi = 0^o$) with maximum gain above 6 dB, 2) desired frequency bandwidth (BW) of ∼12% covering 5.17-5.83 GHz, and 3) linear polarization with axial ratio above 10 dB in the maximum gain direction. Thus, the objective functions are defined as below:

$$\begin{aligned} obj_1 &= Gain(f_i, \theta, \phi) && (Gain \geq 6dB), \\ obj_2 &= BW(|S11|, -10dB) && (BW \geq 12\%), \\ obj_3 &= AR(f_i, \theta, \phi) && (AR \geq 10dB), \end{aligned} \tag{6.1}$$

where $f_i (i = 1, 2, 3)$ represent three frequencies in the 802.11 ac band as 5.17 GHz, 5.5 GHz, and 5.83 GHz, respectively; θ and ϕ describe the desired beam steering direction.

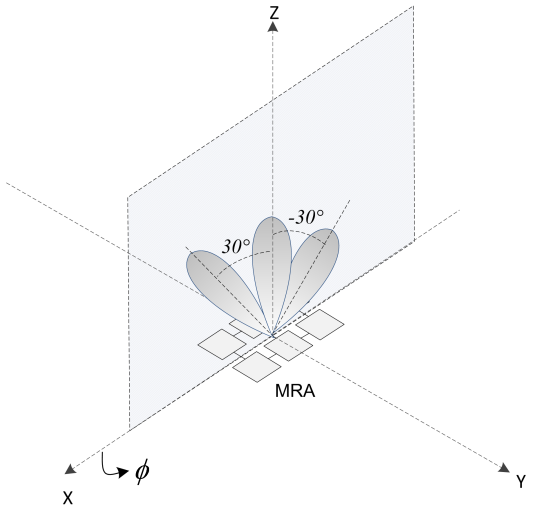

Fig. 6.3: The beam-steering capabilities of an MRA: ($\theta \in \{-30^o, 0^o, 30^o\}\,; \phi = 0^o$).

$|S11|$ represents the magnitude of reflection coefficient, and AR is the axial ratio for polarization. Note that due to the broad band coverage, three frequency points need to be examined to ensure the integrity of the beam steering angle and polarization. These criteria are applied simultaneously in multi-objective genetic algorithm, and in conjunction with full-wave EM analysis to find the optimized switch configurations resulting in each of the three beam steering directions. Also, note that corresponding to beam directions of $(\theta \in \{-30^o, 0^o, 30^o\}\,; \phi = 0^o)$, three optimization problems are defined. The further details of the multi-objective algorithm [30] are omitted here.

6.4 MRA Measurements vs. Simulation

Since there are seven switches between 3×2 rectangular-shaped pixels, the total number of possible switch configurations (i.e. solution space) is only 2^7=128. The number of optimized solutions from the genetic algorithm is therefore even less than 128, and turns out to be ∼20. Thus an expert eye may be used to find the results with the least number of switches for three beam steering directions.

It is finally observed that to achieve three beam steering directions, the required switch number is only two, while all the other switches between pixels are in OFF status. The OFF status switches are then removed from the design (see Fig. 6.1). Note that there are still DC grounding inductors between these pixels although switches are eliminated. The configurations of the switches for three beam steering directions are shown in Table 6.2, where S1 and S2 represent two PIN diode switches used in the design (0 represents the PIN diode is OFF; 1 represents the PIN diode is ON).

A prototype of MRA has been fabricated and measured to validate the results obtained by the theoretical analyses, genetic optimizations and simulations. The prototype generates

Table 6.2: Switch configurations for three beam steering directions.

θ	S1	S2
0^o	0	0
-30^o	1	0
30^o	0	1

three steerable beam directions ($\theta = -30^o, 0^o, 30^o$) on the $\phi = 0^o$ plane. The reflection coefficients of the MRA have been measured. Figures 6.4 and 6.5 show the simulated and measured reflection coefficients for $\theta = 0^o, -30^o, 30^o$ with a common bandwidth covering 802.11 ac band.

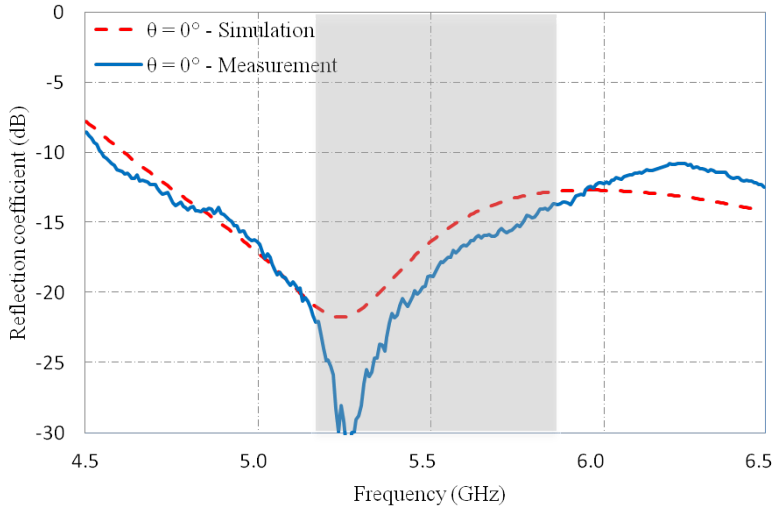

Fig. 6.4: Measured and simulated reflection coefficients of the MRA prototype for beam steering angles $\theta = 0^o$.

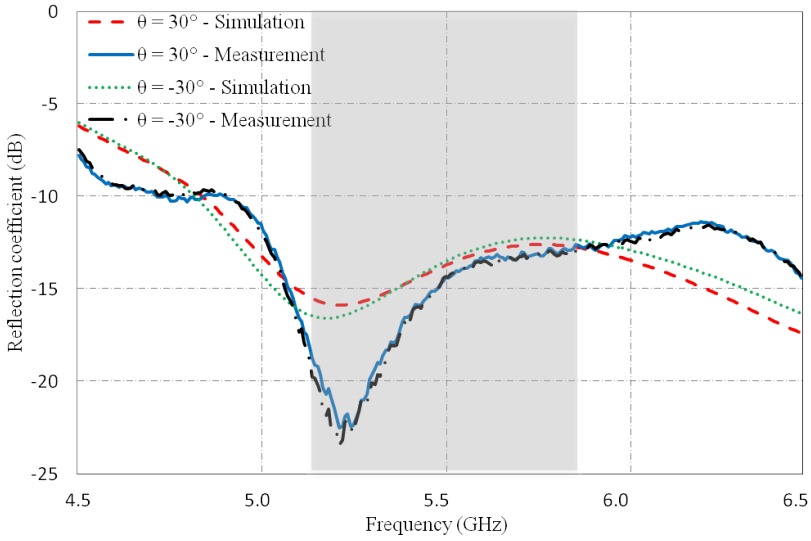

Fig. 6.5: Measured and simulated reflection coefficients of the MRA prototype for beam steering angles $\theta = -30^o$ and $\theta = 30^o$.

The simulated and measured realized gain patterns of the MRA for three beam steering directions at 5.2 GHz, 5.5 GHz, and 5.8 GHz are shown in Fig. 6.6. It is shown that the average maximum gain is ∼6 dB in all the beam steering directions ($\theta \in \{-30^o, 0^o, 30^o\}$; $\phi = 0^o$), and the beam steering angles are maintained over the band.

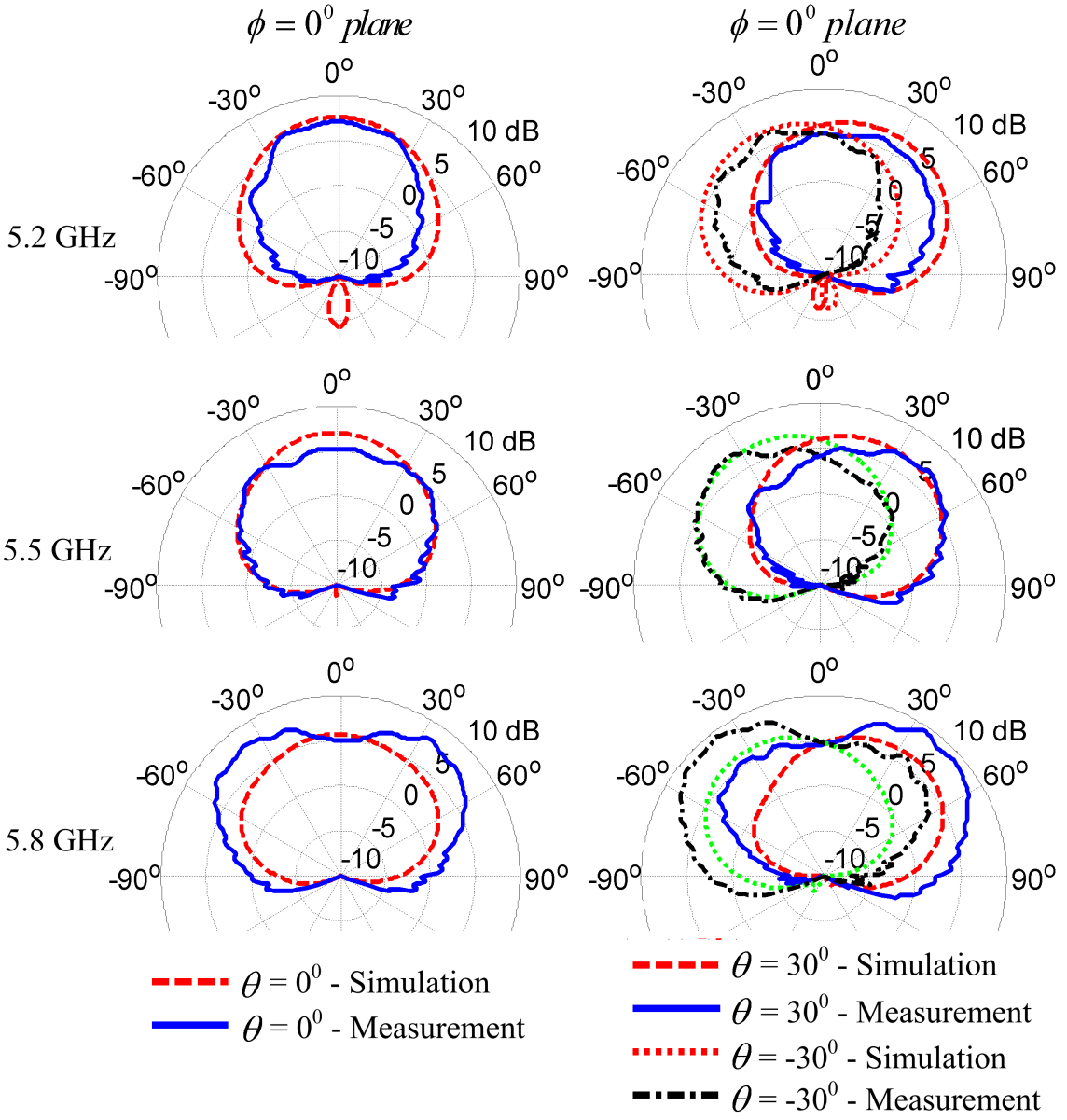

Fig. 6.6: Simulated and measured realized gain patterns of the MRA prototype for beam steering angles $\theta = 0^o$, $\theta = -30^o$ and $\theta = 30^o$ at 5.2 GHz, 5.5 GHz, and 5.8 GHz on $\phi = 0^o$ plane.

6.5 MRAA Design and Measurements

MRAA Structure: As investigated in the previous section, the individual MRA have been designed and optimized by using a multi-objective genetic algorithm in conjunction with full-wave analyses, to generate three modes of operation operating in the 802.11 ac band. The MRAA is then simply formed by the linear combination of four (4×1) identical optimized MRA elements. A 3-D view of the fabricated MRAA is shown in Fig. 6.7. It is fed by a parallel feed network which is shown in the back view of the MRAA in Fig. 6.8. The inter-element spacing between the centers of the adjacent radiators is 30 mm, which is approximately half a wavelength at the frequency of 5.5 GHz (center frequency of 802.11 ac band). This specific spacing between the individual MRA elements has been chosen to reduce the mutual coupling between the individual MRA radiators of the MRAA. Note that the beam-steering plane of the MRA element (x-z plane) is perpendicular to the line along which the MRA elements are aligned (y axis). The realized gain of the MRAA in x-z plane is simply the summation of all the MRA element embedded gains in this plane [40], thus MRAA has the same beam steering capability as MRA in x-z plane but with higher gain. The MRAA has an extended area $(157 \times 80\ mm^2)$ due to array configuration as shown in Fig. 6.7. The feed network, driven stacked patches, parasitic pixel surfaces, and DC bias lines are formed on RO4003C substrates as MRA element.

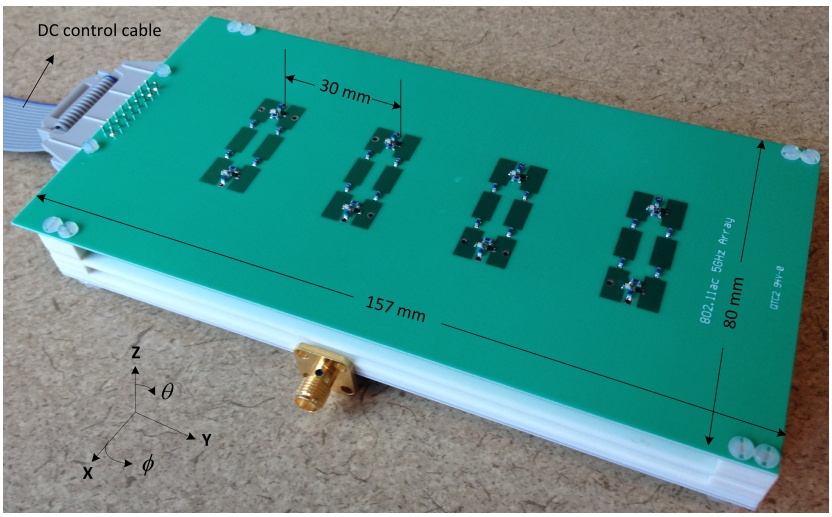

Fig. 6.7: 3-D view of MRAA.

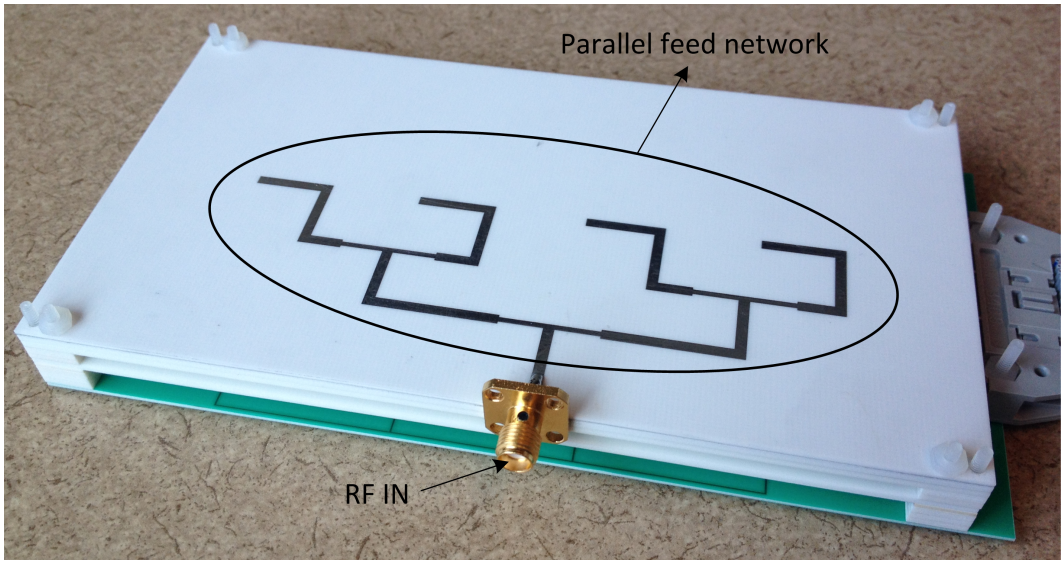

Fig. 6.8: Back view of MRAA.

MRAA Simulation and Measurement Results: To validate the theoretical analyses and simulated results of the MRAA, a prototype of MRAA was fabricated and measured. Three modes of operation ($\theta \in \{-30^o, 0^o, 30^o\}; \phi = 0^o$) are obtained by switching ON/OFF the PIN diode switches through DC bias lines. The MRAA prototype operates in the 802.11 ac frequency band as the individual MRA element. Measurement results agree well with the simulations indicating that the common impedance bandwidth is ∼15% and fully covers the 802.11 ac band as shown in Figs. 6.9 and 6.10.

The simulated and measured realized total gains of all the modes of the MRAA at 5.2 GHz, 5.5 GHz, and 5.8 GHz are shown in Fig. 6.11. It can be seen that the realized gain is on average ∼12 dB over the band in any mode of operation.

It should also be noted that one of the main design challenges of a multi-functional reconfigurable antenna is to simultaneously satisfy all the design requirements. In this case, while the impedance bandwidth fully covers 802.11 ac band, the beam steering capability is maintained over the band. This integrity of beam steering direction vs. frequency makes this MRA suitable for wireless products where the stability of the antenna performance is the main concern.

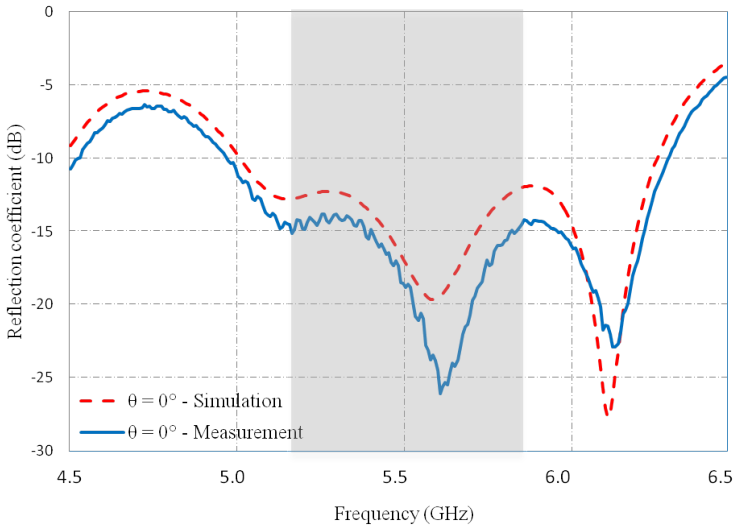

Fig. 6.9: Measured and simulated reflection coefficients of the MRAA prototype for beam steering angles $\theta = 0^o$ on $\phi = 0^o$ plane.

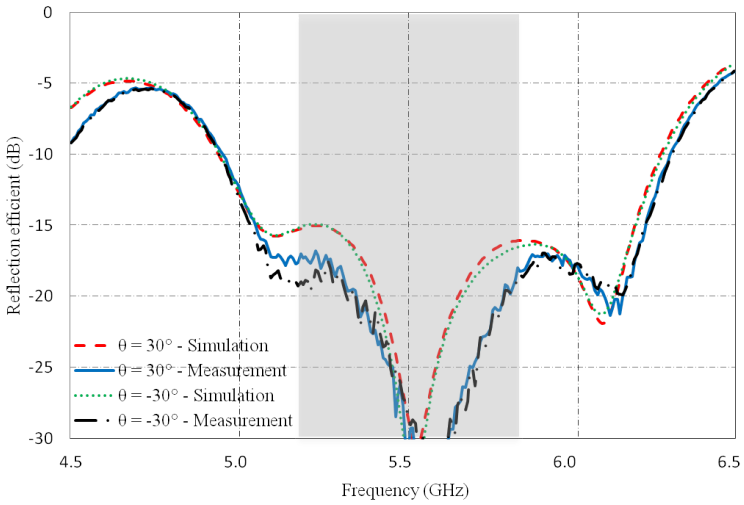

Fig. 6.10: Measured and simulated reflection coefficients of the MRAA prototype for beam steering angles $\theta = 30^o$ and $\theta = -30^o$ on $\phi = 0^o$ plane.

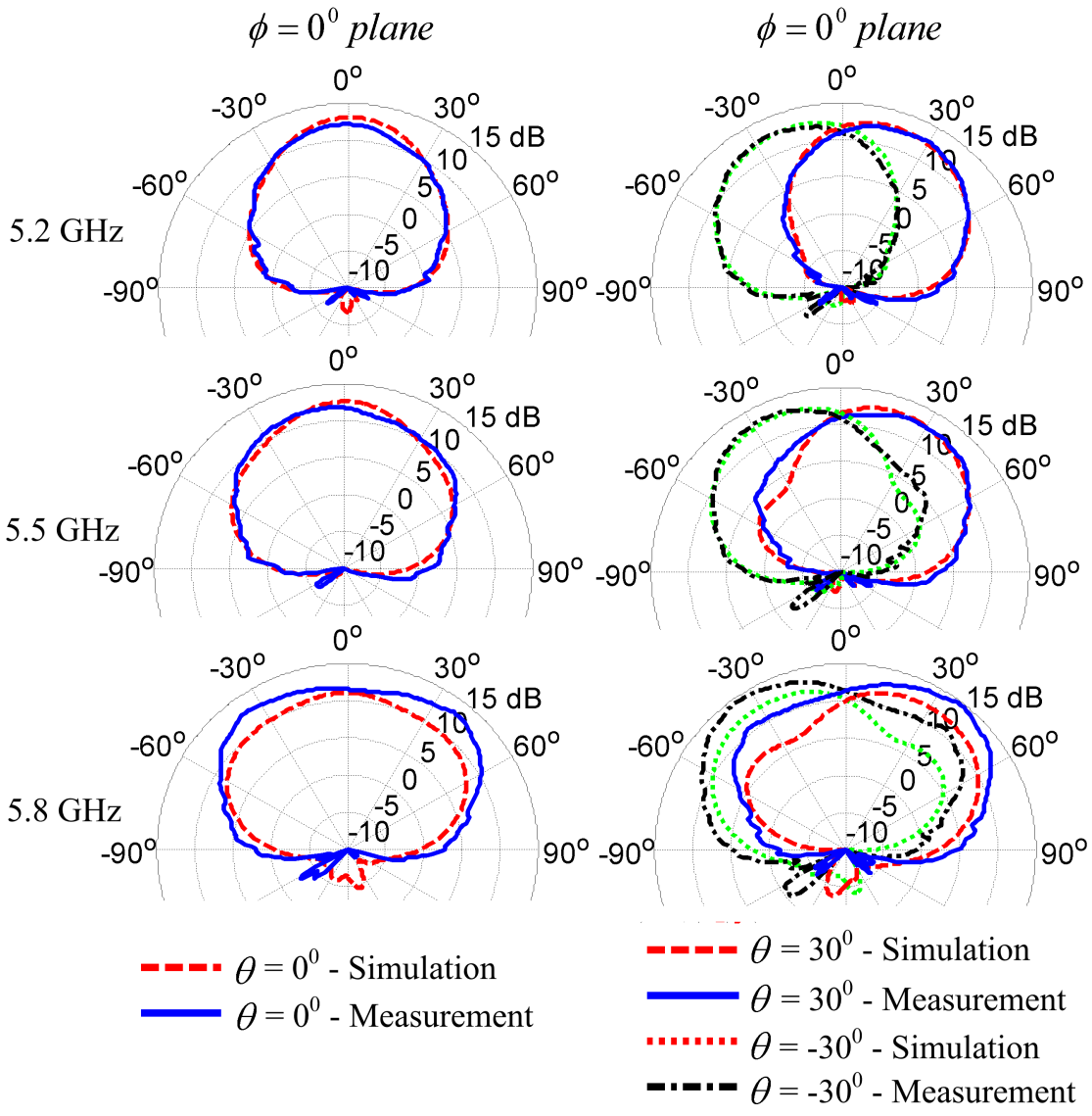

Fig. 6.11: Simulated and measured realized gain patterns of the MRAA prototype for beam steering angles $\theta = 0^o$, $\theta = -30^o$ and $\theta = 30^o$ at 5.2 GHz, 5.5 GHz, and 5.8 GHz on $\phi = 0^o$ plane.

6.6 Conclusions

This chapter presented a full practical model of the multi-functional reconfigurable antenna and array for enhancing the spectral efficiency of IEEE 802.11 ac networks. The MRA and MRAA are capable of steering the beam in three directions ($\theta \in \{-30^o, 0^o, 30^o\}\,; \phi = 0^o$) by reconfiguring the geometry of the parasitic pixel surface. The parasitic surface of a single MRA element consists of a grid of 3×2 electrically small rectangular-shaped metallic

pixels, and the geometry of this surface is altered by switching ON/OFF the two PIN diode switches between the specific metallic pixels. To validate the theoretical analyses and simulations, prototypes of MRA and MRAA operating in the 802.11 ac band have been fabricated and measured. The simulations and measurements of the fabricated MRA (MRAA) prototypes show that the antennas maintain their beam steering capability with a flat maximum realized gain ∼6 dB (∼12 dB) over the whole operational bandwidth.

Chapter 7

Conclusions and Future Work

This dissertation develops the theoretical analysis and design of reconfigurable antennas based on a parasitic layer. The theoretical analysis of the MRA(A) was first investigated to validate the design concept in Chapters 3 and 4, and then applied for practical applications in Chapters 5 and 6. This work developed three MRA(A)s for practical implementation in WLAN systems. The antennas are for practical use in the sense that practical limits have been taken into account with real switches and components implemented. The first prototype is the MRA operating in 802.11 b/g band (2.4-2.5 GHz), with nine beam steering directions in a parasitic layer-based MRA structure. The second is a MRA operating in 802.11ac band (5.17-5.83 GHz) with three beam steering directions in a simplified parasitic layer-based MRA structure. The third is a MRAA extension of the second design. The design process of these MRA(A)s is realized with the joint utilization of electromagnetic (EM) full-wave analysis and multi-objective genetic algorithm. All the MRA(A) designs have been fabricated and measured. The measured and simulated results agree well for both impedance and radiation characteristics. The prototype operating in the 802.11 b/g band was also tested in a 802.11g wireless system and compared with results of a legacy system set-up. The improved performance of MRA based wireless system proves the advantages of the MRA.

The future work based on the current design will focus on development of MRA(A)s with dual frequency operation (2.4-2.5 GHz and 5.17-5.83 GHz). Metallic pixels with different sizes might need to employed to accommodate these two frequencies. In addition, switching circuitry would be necessary on the driven antenna to switch between two operating frequencies. Another choice is to utilize an driven antenna with dual band operation. The antenna will have more reconfigurable modes due to dual frequency operation, but at

the expense of a more complicated structure.

References

[1] B. Cetiner, H. Jafarkhani, J.-Y. Qian, H. J. Yoo, A. Grau, and F. De Flaviis, "Multi-functional reconfigurable mems integrated antennas for adaptive mimo systems," *IEEE Communications Magazine*, vol. 42, pp. 62–70, 2004.

[2] A. Sayeed and V. Raghavan, "Maximizing mimo capacity in sparse multipath with reconfigurable antenna arrays," *IEEE Journal of Selected Topics in Signal Processing*, vol. 1, pp. 156–166, 2007.

[3] D. Piazza, N. Kirsch, A. Forenza, R. Heath, and K. Dandekar, "Design and evaluation of a reconfigurable antenna array for mimo systems," *IEEE Transactions on Antennas and Propagation*, vol. 56, pp. 869–881, 2008.

[4] A. Grau, H. Jafarkhani, and F. De Flaviis, "A reconfigurable multiple-input multiple-output communication system," *IEEE Transactions on Wireless Communications*, vol. 7, pp. 1719–1733, 2008.

[5] H. Eslami, C. Sukumar, D. Rodrigo, S. Mopidevi, A. Eltawil, L. Jofre, and B. Cetiner, "Reduced overhead training for multi reconfigurable antennas with beam-tilting capability," *IEEE Transactions on Wireless Communications*, vol. 9, pp. 3810–3821, 2010.

[6] B. Cetiner, E. Akay, E. Sengul, and E. Ayanoglu, "A mimo system with multifunctional reconfigurable antennas," *IEEE Antennas and Wireless Propagation Letters*, vol. 5, pp. 463–466, 2006.

[7] S. Catreux, V. Erceg, D. Gesbert, and J. Heath, R.W., "Adaptive modulation and mimo coding for broadband wireless data networks," *IEEE Antennas and Wireless Propagation Letters*, vol. 40, pp. 108–115, 2002.

[8] R. J. Mailloux, *Phased Array Antenna Handbook.* Norwood, MA: Artech House, 1994.

[9] W. L. Stutzman and G. A. Thiele, *Antenna Theory and Design,* (2nd ed.). Hoboken, NJ: John Wiley and Sons, 1998.

[10] M. Skolnik, *Radar Handbook,* (2nd ed.). New York: McGraw-Hill Publishing Company, 1990.

[11] D. Parker and D. Zimmermann, "Phased arrays - part 1: Theory and architectures," *IEEE Transactions on Microwave Theory and Techniques*, vol. 50, no. 3, pp. 678 –687, Mar. 2002.

[12] D. Zimmermann and D. Parker, "Phased arrays-part 2: Implementations, applications, and future trends," *IEEE Transactions on Microwave Theory and Techniques*, vol. 50, no. 3, pp. 688 –698, Mar. 2002.

[13] C. Panagamuwa, A. Chauraya, and J. Vardaxoglou, "Frequency and beam reconfigurable antenna using photoconducting switches," *IEEE Transactions on Antennas and Propagation*, vol. 54, no. 2, pp. 449–454, Feb. 2006.

[14] J. Kiriazi, H. Ghali, H. Ragaie, and H. Haddara, "Reconfigurable dual-band dipole antenna on silicon using series mems switches," in *Antennas and Propagation Society International Symposium, IEEE*, pp. 403–406, June 2003.

[15] E. Erdil, K. Topalli, M. Unlu, O. Civi, and T. Akin, "Frequency tunable microstrip patch antenna using rf mems technology," *IEEE Transactions on Antennas and Propagation*, vol. 55, no. 4, pp. 1193 –1196, Apr. 2007.

[16] S. Shynu, G. Augustin, C. Aanandan, P. Mohanan, and K. Vasudevan, "C-shaped slot loaded reconfigurable microstrip antenna," *Electronics Letters*, vol. 42, no. 6, pp. 316–318, Mar. 2006.

[17] M. Fries, M. Grani, and R. Vahldieck, "A reconfigurable slot antenna with switchable polarization," *IEEE Microwave and Wireless Components Letters*, vol. 13, no. 11, pp. 490–492, Nov. 2003.

[18] P. Rainville and F. Harackiewicz, "Magnetic tuning of a microstrip patch antenna fabricated on a ferrite film," *IEEE Microwave and Guided Wave Letters*, vol. 2, no. 12, pp. 483–485, Dec. 1992.

[19] D. Pozar and V. Sanchez, "Magnetic tuning of a microstrip antenna on a ferrite substrate," *Electronics Letters*, vol. 24, no. 12, pp. 729–731, June 1988.

[20] R. Mishra, S. Pattnaik, and N. Das, "Tuning of microstrip antenna on ferrite substrate," *IEEE Transactions on Antennas and Propagation*, vol. 41, no. 2, pp. 230–233, Feb. 1993.

[21] A. Brown, J. Volakis, L. Kempel, and Y. Botros, "Patch antennas on ferromagnetic substrates," *IEEE Transactions on Antennas and Propagation*, vol. 47, no. 1, pp. 26–32, Jan. 1999.

[22] S.-L. Yang and K.-M. Luk, "Design of a wide-band l-probe patch antenna for pattern reconfiguration or diversity applications," *IEEE Transactions on Antennas and Propagation*, vol. 54, no. 2, pp. 433–438, Feb. 2006.

[23] D. Sievenpiper, J. Schaffner, R. Loo, G. Tangonan, S. Ontiveros, and R. Harold, "A tunable impedance surface performing as a reconfigurable beam steering reflector," *IEEE Transactions on Antennas and Propagation*, vol. 50, no. 3, pp. 384–390, Mar. 2002.

[24] D. Sievenpiper, J. Schaffner, H. Song, R. Loo, and G. Tangonan, "Two-dimensional beam steering using an electrically tunable impedance surface," *IEEE Transactions on Antennas and Propagation*, vol. 51, no. 10, pp. 2713–2722, Oct. 2003.

[25] D. Sievenpiper, J. Schaffner, J. Lee, and S. Livingston, "A steerable leaky-wave antenna using a tunable impedance ground plane," *IEEE Antennas and Wireless Propagation Letters*, vol. 1, no. 1, pp. 179–182, 2002.

[26] D. Sievenpiper and J. Schaffner, "Beam steering microwave reflector based on electrically tunable impedance surface," *Electronics Letters*, vol. 38, no. 21, pp. 1237–1238, Oct. 2002.

[27] D. Sievenpiper, "Forward and backward leaky wave radiation with large effective aperture from an electronically tunable textured surface," *IEEE Transactions on Antennas and Propagation*, vol. 53, no. 1, pp. 236–247, Jan. 2005.

[28] R. Harrington, "Reactively controlled directive arrays," *IEEE Transactions on Antennas and Propagation*, vol. 26, no. 3, pp. 390–395, May 1978.

[29] Z. Li, H. Mopidevi, O. Kaynar, and B. Cetiner, "Beam-steering antenna based on parasitic layer," *Electronics Letters*, vol. 48, no. 2, pp. 59–60, Jan. 2012.

[30] X. Yuan, Z. Li, D. Rodrigo, H. Mopidevi, O. Kaynar, L. Jofre, and B. Cetiner, "A parasitic layer-based reconfigurable antenna design by multi-objective optimization," *IEEE Transactions on Antennas and Propagation*, vol. 60, no. 6, pp. 2690–2701, June 2012.

[31] J. Papapolymerou and J. Bernhard, "Special issue on multifunction antennas and antenna systems," *IEEE Transactions on Antennas and Propagation*, vol. 54, no. 2, pp. 314–316, 2006.

[32] B. Cetiner, J. Qian, H. Chang, M. Bachman, G. P. Li, and F. De Flaviis, "Monolithic integration of rf mems switches with a diversity antenna on pcb substrate," *IEEE Transactions on Microwave Theory and Techniques*, vol. 51, no. 1, pp. 332–335, 2003.

[33] L. Pringle, P. Harms, S. Blalock, G. Kiesel, E. Kuster, P. Friederich, R. Prado, J. Morris, and G. Smith, "A reconfigurable aperture antenna based on switched links between electrically small metallic patches," *IEEE Transactions on Antennas and Propagation*, vol. 52, no. 6, pp. 1434–1445, 2004.

[34] D. Rodrigo, Y. Damgaci, M. Unlu, B. Cetiner, J. Romeu, and L. Jofre, "Antenna reconfigurability based on a novel parasitic pixel layer," in *Antennas and Propagation (EUCAP), Proceedings of the 5th European Conference*, pp. 3497–3500, 2011.

[35] Synthetic quartz glass substrates. Shin-Etsu Chemical Co. [Online]. Available: http://www.shinetsu.co.jp

[36] K. Deb, A. Pratap, S. Agarwal, and T. Meyarivan, "A fast and elitist multiobjective genetic algorithm: Nsga-ii," *IEEE Transactions on Evolutionary Computation*, vol. 6, no. 2, pp. 182–197, 2002.

[37] Ansoft hfss version 11.0. ANSIS Corporation, July 2007. [Online]. Available: http://www.ansys.com

[38] J. T. Bernhard, "Reconfigurable antennas," *Synthesis Lectures on Antennas*, 2007.

[39] E. Brown, "On the gain of a reconfigurable-aperture antenna," *IEEE Transactions on Antennas and Propagation*, vol. 49, no. 10, pp. 1357 –1362, Oct. 2001.

[40] Z. Li, D. Rodrigo, L. Jofre, and B. Cetiner, "A new class of antenna array with a reconfigurable element factor," *IEEE Transactions on Antennas and Propagation*, vol. 61, no. 4, pp. 1947–1955, 2013.

[41] ROHACELL HF foam. Evonik Industries. [Online]. Available: www.evonik.com

[42] Y. Kuwahara, "Multi-objective optimization design of yagi-uda antenna," *IEEE Transactions on Antennas and Propagation*, vol. 53, no. 6, pp. 1984–1992, June 2005.

[43] D. Boeringer and D. Werner, "Be'zier representations for the multi-objective optimization of conformal array amplitude weights," *IEEE Transactions on Antennas and Propagation*, vol. 54, no. 7, pp. 1964–1970, July 2006.

[44] J. Petko and D. Werner, "The pareto optimization of ultrawideband polyfractal arrays," *IEEE Transactions on Antennas and Propagation*, vol. 56, no. 1, pp. 97–107, Jan. 2008.

[45] SMP 1345 series. Skyworks Co. 2014. [Online]. Available: http://www.skyworksinc.com

[46] HP 0603. Coilcraft Co. 2013. [Online]. Available: http://www.coilcraft.com

[47] GQM 0603. Murata Co. 2014. [Online]. Available: http://www.murata.com

[48] Universal software radio peripheral (usrp) datasheet, 2012. [Online]. Available: https://www.ettus.com/product/category/USRP-Networked-Series

[49] The Zedboard. [Online]. Available: http://www.zedboard.org

[50] IEEE standard for information technology-telecommunications and information exchange between systems local and metropolitan area networks-specific requirements part 11: Wireless lan medium access control (mac) and physical layer (phy) specifications. IEEE Std 802.11-2012 (Revision of IEEE Std 802.11-2007).

[51] H. Mahmoud and H. Arslan, "Error vector magnitude to snr conversion for nondata-aided receivers," *IEEE Transactions on Wireless Communications*, vol. 8, no. 5, pp. 2694–2704, May 2009.

[52] J. F. Zurcher and F. E. Gardiol, *Broadband Patch Antennas.* Norwood, MA: Artech House, 1995.

[53] S. D. Targonski and D. M. Pozar, "Design of wideband circularly polarized aperture-coupled microstrip antennas," *IEEE Transactions on Antennas and Propagation*, vol. 41, no. 2, pp. 214–220, Feb. 1993.

[54] C. Chen, A. Tulintseff, and R. Sorbello, "Broadband two-layer microstrip antenna," in *Antennas and Propagation Society International Symposium*, vol. 22, pp. 251–254, June 1984.

[55] F. Croq and D. M. Pozar, "Millimeter-wave design of wide-band aperture-coupled stacked microstrip antennas," *IEEE Transactions on Antennas and Propagation*, vol. 39, no. 12, pp. 1770–1776, Dec. 1991.

[56] G. Kumar and K. Gupta, "Broad-band microstrip antennas using additional resonators gap-coupled to the radiating edges," *IEEE Transactions on Antennas and Propagation*, vol. 32, no. 12, pp. 1375–1379, Dec. 1984.

[57] D. Rodrigo, B. Cetiner, and L. Jofre, "Frequency, radiation pattern and polarization reconfigurable antenna using a parasitic pixel layer," *IEEE Transactions on Antennas and Propagation*, vol. 62, no. 6, pp. 3422–3427, June 2014.

Vita

Zhouyuan Li

Journal Articles

- A new class of antenna array with a reconfigurable element factor, Z. Li, D. Rodrigo, L. Jofre, B. A. Cetiner, *IEEE Transactions on Antennas and Propagation*, vol. 61, no. 4, pp. 1947-1955, Apr. 2013.
- Beam-steering antenna based on parasitic layer, Z. Li, H. Mopidevi, O. Kaynar, B. A. Cetiner, *IEE Electronics Letters*, vol. 48, pp. 59-60, 2012.
- A parasitic layer-based reconfigurable antenna design by multi-objective optimization, X. Yuan, Z. Li, D. Rodrigo, H. S. Mopidevi, O. Kaynar, L. Jofre and B. A. Cetiner, *IEEE Transactions on Antennas and Propagation*, vol. 60, no. 6, pp. 2690-2701, June 2012.
- A beam-steering reconfigurable antenna for WLAN applications, Z. Li, E. Ahmed, A. M. Eltawil, B. A. Cetiner, under revision, *IEEE Transactions on Antennas and Propagation*
- A broadband beam-steering reconfigurable antenna, Z. Li and B. A. Cetiner, to be submitted.